Nanoscale

PAPER

View Article Online
View Journal | View Issue

Cite this: *Nanoscale*, 2025, **17**, 7926

Functionalized graphitic carbon nitride as an efficient electro-analytical platform for the label-free electrochemical sensing of interleukin-8 in saliva samples†

Sumit K. Yadav,‡[a,b] Amit K. Yadav, ‡[a] Ajeet Kaushik [c] and Pratima R. Solanki *[a]

A correlation between the emerging high case fatality rate of head and neck cancer and its propensity to migrate metastatically to other parts of the body makes it a significant global danger. It raises the demand for low-level detection, which is useful for early-stage diagnostics. Graphitic carbon nitride (g-C_3N_4) has recently garnered considerable attention as a promising nanomaterials for biosensor due to its exceptional redox behavior, electrochemical activity, and abundance of electroactive sites. The current study presents research outcomes regarding the development of an ultra-sensitive platform for detecting interleukin-8 (IL8), a cytokine associated with oral cancer. This investigation involves fabricating the platform using 3-aminopropyl trimethoxysilane (APTES)-functionalized g-C_3N_4 and assessing its efficacy in both laboratory-made and real samples. The process of g-C_3N_4 synthesis involved the thermal pyrolysis of urea without any add-on material. Moreover, the APTES@g-C_3N_4 nanomaterial was subjected to electrophoretic deposition onto an ITO-coated glass electrode. The fabricated APTES@g-C_3N_4/ITO electrode was covalently immobilized by the EDC and NHS chemical reaction in conjunction with anti-interleukin-8 (anti-IL8) antibodies. Before using these sensors for interleukin-8 (IL8) sensing, the anti-IL8/APTES@g-C_3N_4/ITO electrode was treated with bovine serum albumin (BSA) molecules utilized to obstruct non-targeted areas. Such a fabricated BSA/anti-IL8/APTES@g-C_3N_4/ITO electrochemical immunosensing bioelectrode was characterized by various analytical, morphological, and electrochemical techniques to confirm the stepwise fabrication of the sensor. BSA/anti-IL8/APTES@g-C_3N_4/ITO demonstrates a noticeable DPV based electrochemical response as a function of IL8 in the concentration ranging from 500 fg mL^{-1} to 160 ng mL^{-1}. This BSA/anti-IL8/APTES@g-C_3N_4/ITO also exhibits a lower limit of detection (LOD) of 0.04 ng mL^{-1}, a sensitivity of 0.015 mA $\log_{10}$ [ng mL^{-1}] cm^{-2}, and stability for up to 10 weeks. The biosensor demonstrates excellent performance in analyzing real samples, indicating its practical utility. This efficacy can be attributed to the abundance of electroactive sites, confined electronic structures, and strong interactions among the active g-C_3N_4 matrix, anti-IL8 molecules, and IL8 molecules. Our findings are essential for advancing early and point-of-care diagnostics, where quick turnaround times and great sensitivity are critical.

Received 11th May 2024,
Accepted 27th June 2024

DOI: 10.1039/d4nr02039a

rsc.li/nanoscale

1 Introduction

Oral cancer (OC) represents a distinct category within the spectrum of head and neck malignancies, encompassing neoplastic epithelial growths affecting the oral cavity, nasal cavity, oropharynx, paranasal sinuses, and larynx, with a predominant incidence exceeding 90% it manifests within the latter three anatomical regions.[1,2] Globally, occlusion cerebri has emerged as a significant public health challenge.[3–5] According to estimates from the American Cancer Society, in 2017 alone, there were 49 670 new OC cases reported, leading to the loss of 9700 lives in the United States.[6] Cancer biomarkers, encompassing proteins, enzymes, DNA, and mRNA, represent a unique cohort of biological entities whose manifestation in cells, tissues, or bodily fluids indicates cancerous processes.[7] Real-time quantifiable tracking of these biomarkers is essential for timely disease detection, individualized treatment strategizing, and evaluation of treatment effectiveness.[8] Interleukin-8 (IL8), a cytokine implicated in angiogenesis and cellular proliferation processes across diverse cancer phenotypes, holds sig-

[a]*NanoBio Laboratory, Special Center for Nanoscience, Jawaharlal Nehru University, New Delhi-110067, India. E-mail: partima@mail.jnu.ac.in, pratimarsolanki@gmail.com; Tel: +011-26704740/26704699*
[b]*University Department of Biotechnology, Vinoba Bhave University, Hazaribagh, Jharkhand 825301, India*
[c]*NanoBioTech Laboratory, Department of Environmental Engineering, Florida Polytechnic University, Lakeland 33805, FL, USA*
†Electronic supplementary information (ESI) available. See DOI: https://doi.org/10.1039/d4nr02039a
‡These authors contributed equally to this work.

nificant relevance in this context (the complete amino acid sequence of IL8 protein is provided in ESI S1†).[9,10] Studies have shown elevated IL8 levels in saliva samples from OC patients (720 pg mL^{-1}) compared to unaffected individuals (250 pg mL^{-1}).[11] Consequently, analyzing saliva's IL8 levels offers a non-invasive approach for early OC detection, rendering it a valuable diagnostic tool.

The management of cytokines, which play a crucial role in immune response, necessitates rapid and accurate detection methods, particularly in diagnosing and treating conditions like cancers.[12] The survival rate for OC remains low despite considerable advancements in diagnostic and treatment techniques. The disease's delayed diagnosis is one of the main reasons why treatment approaches don't work. The disease cannot be detected until it has progressed to an advanced stage by conventional techniques such as surface-enhanced Raman spectroscopy, gel electrophoresis, mass spectrometry, enzyme-linked immunosorbent assay (ELISA), and fluorescence assay.[13,14] These technologies offer dependable and precise results, but they are not suitable substitutes because of issues with sensitivity, sample size, detection time, expenditure on instrumentation, and the requirement for proficient personnel.[15,16] The development of sophisticated point-of-care (POC) screening modalities aimed at early detection of OC can significantly boost the treatment efficacy and lower the death rate from this terrible illness. POC sensing addresses traditional issues by providing immediate, on-site results, which is vital for timely decision-making in acute and emergency situations. The portability and accessibility of POC devices allow for advanced diagnostics in remote or resource-limited settings, expanding healthcare reach. The integration of POC cytokine sensors into clinical practice thus promises to enhance patient outcomes by improving the efficiency and precision of cytokine management. For clinical diagnosis, electrochemical immunosensing has shown to be a straightforward, quick, affordable, and portable monitoring technique for biomarker quantification.[17,18] Immunosensors are important because they can provide real-time and accurate data in situations where current methods may have gaps or limitations. These can be especially valuable in the field of healthcare monitoring, where timely and precise information is essential for making informed decisions. However, it is crucial to choose bioreceptor and transducer matrices that meet several critical criteria: reliability, biocompatibility, a high surface-to-volume ratio, electrochemical activity, and a rapid electron transfer rate. These factors are essential for creating sensitive and accurate electrochemical biosensing systems.

The successful development of biosensors has extensively used various metals and metal-based nanomaterials, including oxides,[19–21] sulfides,[22,23] selenides,[24,25] and carbides.[26,27] However, expensive and hazardous precursors with considerable molecular weights are used to synthesize these metal-based nanomaterials. Furthermore, many of these metal complexes have a propensity to aggregate and may diminish their dispersion ability. Carbonaceous nanomaterials, such as carbon allotropes like graphene and its derivatives, notably oxides of graphene,[28–30] multi-walled carbon nanotubes,[31,32] porous carbon, carbon nanofibers,[33] *etc.*, offer a solution to this challenge. These nanomaterials possess exceptional properties, including their structural integrity and thermal and electrical conduction capacity, electron transport capabilities, and biocompatibility. Considerable research efforts have been focused on studying new carbon-based nanomaterials for biosensing. Among these, graphitic carbon nitride (g-C_3N_4) stands out as a promising candidate.[33] g-C_3N_4, one of the carbon nitride allotropes, is highly stable and exhibits unique optical and photoelectrochemical properties. This compound features $-NH_2$ or –NH moieties, which serve as catalysts facilitating the formation of –H covalent bonds with various functional groups, including –OH, –COOH, or –SH.[34–37] g-C_3N_4 nanomaterials are semiconductor polymers with a structure ranging from polymeric to graphitic characterized by a prominent nitrogen to carbon ratio (N : C ratio = 3/4) alongside a limited hydrogen content. This configuration resembles graphite with nitrogen-substituted sp^2-hybridized graphene, earning it the designation "graphitic" due to its layered structure and weak interlayer *van der Waals* forces.[38] Due to its nominal bandgap of 2.7 eV, this emerging carbonaceous nanomaterial has recently attracted attention. It has a porous structure with electron-rich characteristics and simple surface functions that facilitate the compound's easy biofunctionalization. However, its physicochemical stability, biocompatibility, environmental friendliness, and cost-effectiveness direct it toward biomedical uses such antibacterial, therapeutic, and diagnostic applications.[39–43]

At the moment, doctors lack a straightforward, quick, or less invasive diagnostic tool that would enable them to identify cancer at the POC and customize treatment accurately. Thus, there is a pressing need to create biosensors that can quickly and affordably measure a salivary cytokine profile correctly and serve as biological markers for cancer diagnosis. The doctor will use saliva testing to identify cancer-specific cytokine signatures early on, enabling quick diagnosis and tailored treatment as needed. No label-free g-C_3N_4-based electrochemical biosensor has been documented to measure salivary cytokines (IL8) to detect OC directly.

This study introduces a novel and scalable approach for the rational design of APTES-functionalized g-C_3N_4 nanosheet-based electrodes aimed at sensitive and label-free POC detection of the OC biomarker IL8 in saliva samples. Leveraging the highly conductive nature of g-C_3N_4 nanosheets, it facilitate rapid electron transfer, resulting in superior sensing capabilities. Notably, the APTES@g-C_3N_4 composite demonstrates a robust coupling interaction between anti-IL8 and g-C_3N_4, augmenting active sites and enhancing electron-transfer kinetics. This enhanced electron transport is attributable to the exceptional electrical conductivity and expansive surface area of g-C_3N_4. The optimized BSA/anti-IL8/APTES@g-C_3N_4/ITO biosensor exhibit remarkable sensing performance toward IL8, featuring high selectivity, sensitivity (0.015 mA $\log_{10}$ [ng mL^{-1}] cm^{-2}), a broad linear detection range (500 fg mL^{-1}–160 ng mL^{-1}), a low detection limit at the femtomolar level (0.04 ng

mL^{-1}), exceptional reproducibility, and prolonged stability. Importantly, the sensing capabilities of this developed biosensors surpass those of state-of-the-art IL8 biosensors reported in the literature (Table 3). Moreover, here demonstrate the practical applicability of approach by achieving satisfactory recovery rates in detecting IL8 in real samples, showcasing tremendous sensing performance. This research addresses a significant gap in the current diagnostic methodologies for cancer and inflammatory diseases, offering a promising alternative that combines accuracy, efficiency, and patient convenience. The development of such advanced diagnostic tools is crucial for enhancing disease management and overall healthcare delivery. This methodology offers a novel avenue for detecting various disease markers.

2 Experimental section

2.1 Chemicals and reagents

All chemical compounds and reagents employed in the current study, including ethanol (CH_3CH_2OH, ≥99.9%), acetone (CH_3COCH_3, ≥99.9%), sodium hydroxide pellets (NaOH), potassium hexacyanoferrate(III) ($K_3[Fe(CN)_6]$, 99%), bovine serum albumin (BSA, ≥96%), ammonium hydroxide solution (NH_4OH), hydrogen peroxide (H_2O_2), *N*-ethyl-*N*′-(3-dimethyl aminopropyl) carbodiimide hydrochloride (EDC, $C_8H_{17}N_3$, ≥97.0%), potassium hexacyanoferrate(II) trihydrate ($K_4[Fe(CN)_6]\cdot 3H_2O$, ≥99.95%), *N*-hydroxy succinimide (NHS, ≥98%), (3-aminopropyl) trimethoxysilane (APTES, 99%), acetonitrile (ACN, CH_3CN, ≥99.9%), sodium phosphate dibasic dihydrate ($Na_2HPO_4\cdot 2H_2O$, ≥99.0%), *N,N*-dimethylformamide (DMF), ascorbic acid ($C_6H_8O_6$, 99.7%), sodium phosphate monobasic anhydrous (NaH_2PO_4, ≥98%), sodium chloride (NaCl, ≥99.0%), urea (NH_2CONH_2, 99.5%), and uric acid ($C_5H_4N_4O_3$, 99%), were procured from reputable suppliers including Sigma Aldrich, SRL Limited, Fisher Scientific, and Hi-Media. PBS with a pH of 7.0 was employed to dilute specific interleukin-8 (IL8) and interleukin-8 antibodies (anti-IL8) sourced from Abcam, United Kingdom. Additional proteins such as sperm protein 17 (Sp17), tumor necrosis factor-alpha, and CYFRA-21-1 were obtained from MyBioSource, USA. The purchase of indium tin oxide ITO (indium tin oxide)-coated glass was made at Blazers in the United Kingdom (UK). Fresh phosphate buffer solution (PBS) was prepared using NaH_2PO_4 and $Na_2HPO_4\cdot 2H_2O$ in distilled water (DI) to have a pH of 7.0. It was then stored at 4 °C for the duration of the experiment. Furthermore, the entire experiment was run in deionized water (DI). In every study, Milli-Q-water (18.2 MΩ cm@ 25 ± 2 °C) was utilized. DI water was obtained from Milli Q, a Millipore unit (Elix USA) of 18.2 MΩ resistance. The corresponding compounds were utilized unaltered and of analytical quality, requiring no further processing.

2.1.1 Materials characterization. The investigation into the morphological, chemical, and surface characteristics of the synthesized g-C_3N_4 involved the use of Scanning Electron Microscopy (SEM, JSM-IT 200, JEOL, Japan) and Transmission Electron Microscopy (HR-TEM, JEM-2200 FS, Jeol, Japan) along with the examination of selected-area electron diffraction (SAED) patterns. Energy dispersive spectroscopy (EDS, JSM-IT 200, JEOL) was employed for chemical and elemental composition analyses. Crystallinity assessment was carried out using X-ray diffraction spectroscopy (XRD, Rigaku Miniflex 600 (Japan) diffractometer) with Cu Kα radiation, with data processed using EVA software. Functional group analysis was conducted using attenuated total reflection Fourier transform infrared spectroscopy (ATR-FT-IR spectrophotometer, PerkinElmer, US) spanning wavenumbers from 4000 to 400 cm^{-1}. The Raman spectra of the materials were recorded in the 500–2000 cm^{-1} range using a laser source of 633 nm excitation wavelength (EnSpectr R532, the USA) with a confocal microscope. Contact angle measurements were performed using a drop shape analyzer (KRUSS, Germany) to determine electrode surface wettability distinguishing between hydrophilicity and hydrophobicity. Sonication of g-C_3N_4 was carried out using an ultrasonic probe Vibra Cell™ (Sonics) operating at 130 W and 20 kHz, followed by centrifugation using an Eppendorf Sorvall ST16 centrifuge.

2.1.2 Electrochemical characterization. The prepared electrodes were electrochemically evaluated with an Autolab Potentiostat/Galvanostat electrochemical analyzer based on a three-electrode system design using the traditional electrode configuration (EcoChemie, The Netherlands). Specifically, ITO electrodeposited on a glass substrate was used as the working electrode, platinum as the counter electrode, and Ag/AgCl as the reference electrode. Cyclic voltammetry (CV) and differential pulse voltammetry (DPV) were performed using NOVA 1.10 software for data acquisition. All electrochemical experiments were performed at room temperature (RT). CV and DPV measurements were carried out in PBS containing 5 mM redox species. In the context of CV measurements, the electrochemical potential underwent scanning within the voltage window of −0.8 to +0.8 volts at a scan rate of 50 mV s^{-1}. Three separate comprehensive electrochemical analyses were carried out (n = 3). In addition, a reference was used to monitor and control the solution's oxygen concentration while determining the electrochemical cell's potential. Potential monitoring allowed for detecting and rectifying any deviations ascribed to oxygen interference.

2.2 Synthesis and functionalization of g-C_3N_4

According to the literature-reported methodology, g-C_3N_4 was synthesized by simple pyrolysis of urea at 550 °C.[44] 10 g of desiccated urea was weighed and placed within a covered crucible. After that, the sample was heated to 550 °C at 175 °C per hour in a muffle furnace. The sample was heated for 4 hours at 550 °C and then cooled to RT. Following the chemical reaction, observation revealed the formation of a pale-yellow precipitate within the crucible, which was subsequently collected, centrifuged at 8000 rpm, repeatedly cleaned with ethanol and water, and left to dry overnight at 80 °C. To obtain g-C_3N_4 as a powder composite, the dried powder was further ground with a mortar and pestle. The resultant product was gathered in an

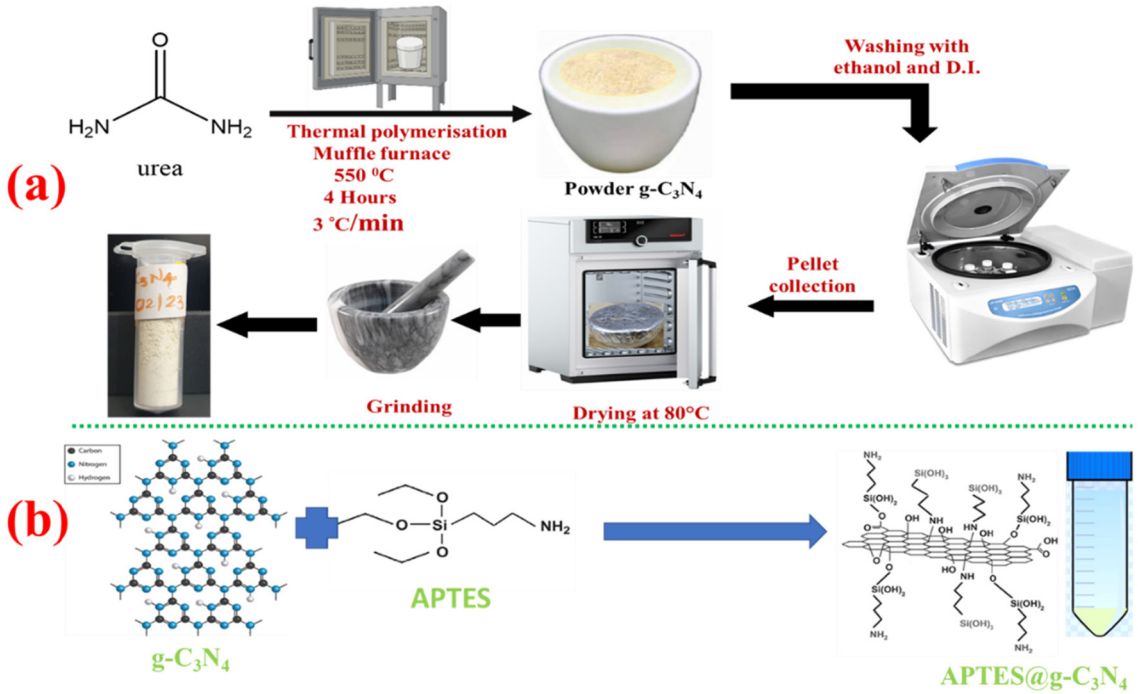

Scheme 1 A schematic depiction of the stepwise procedure involving (a) the synthesis and (b) the APTES functionalization of g-C_3N_4 aimed at creating a biosensing platform.

Eppendorf tube and vacuum-sealed for later use. Scheme 1(a) provides an illustrative depiction representing the comprehensive synthesis process of g-C_3N_4. Before the material could be employed for IL8 sensing applications, it was necessary to validate the successfully synthesized material using various analytical characterization techniques.

A linker was employed to immobilize the functional components onto the surface of the g-C_3N_4 to bioconjugate the corresponding protein molecule. For this purpose, a silane coupler termed 3-aminopropyltriethoxysilane (APTES) with amino functionality was used. As demonstrated in Scheme 1(b), the triethoxy group at one end undergoes direct hydrolysis with the amine group at the other end, facilitating attachment to the surface of the matrix. This demonstrates that APTES is a very promising linking agent.[45] Next, at 60 °C and 400 rpm, a g-C_3N_4 (10 mg) solution in 10 mL of isopropanol was continuously stirred. To this dispersion, 200 μL of 98% APTES was added and vigorously agitated for 48 hours at 300 rpm. After the triethoxy group [$(OC_2H_5)_3$–Si–$(CH_2)_3NH_2$] hydrolysis, reactive [$(OH)_3$–Si–$(CH_2)_3NH_2$] trisilanol groups were created. These groups then covalently bonded to the g-C_3N_4 basal plane surface, allowing the amino silane group to be grafted to the g-C_3N_4 nanomaterial.

Moreover, the APTES-free amine terminus was utilized to link a protein to the g-C_3N_4 surface covalently. To synthesize APTES-functionalized g-C_3N_4 (APTES@g-C_3N_4), the resultant material underwent purification using Mili-Q water to eliminate the residual APTES. Subsequently, it was subjected to drying at 60 °C and stored in a dried environment. Using a mortar and pestle, the product was pounded into a fine powder for later use.

2.3 Electrophoretic deposition

Glass substrates coated with ITO, each measuring 1.5 × 0.5 cm, underwent hydrolyzation before use. The ITO sheets were meticulously cleaned *via* sonication in acetone, followed by a soap solution, and finally ultra-pure water, each for 10 min. Subsequently, the cleaned ITO sheets were subjected to incubation at 80 °C for 1 h in a solution comprising H_2O_2/NH_4OH/H_2O (in a ratio of 1 : 1 : 5). After rinsing with ultra-pure water and ethanol, the electrodes were dried at 60 °C in an oven. A stock solution of APTES@g-C_3N_4 (1 mg mL^{-1}) was prepared by ultrasonication with 1 mg of the material dissolved in 1 mL of DMF before electrophoretic deposition (EPD). The EPD process involved positioning the working electrode (ITO) and reference electrode (platinum wire) separated by a distance of 1 cm within a glass cell. The surface area of the APTES@g-C_3N_4/ITO platforms was systematically optimized and quantified, revealing an optimal surface area of 0.25 cm^2.

Subsequently, a glass cell was filled with an optimized solution consisting of 4 mL acetonitrile, 100 μL of the APTES-functionalized g-C_3N_4 stock solution, and 20 μL of $Mg(NO_3)_2$, followed by 60 s of ultrasonic sonication. The deposition of APTES@g-C_3N_4 onto the ITO substrate, pre-treated with hydrolysis, was performed using an EPD approach employing a Genetix GX300C instrument. A direct current (DC) voltage of 60 V was administered for a duration of 2 min, ensuring the uniform deposition of a thin layer of APTES@g-C_3N_4 on the ITO electrode

(APTES@g-C_3N_4/ITO) after optimization, as summarized in Table S1.† Finally, the developed electrode underwent cleaning with Mili-Q water and was left to dry overnight at 25 °C.

2.4 Development of the immunosensor platform

The APTES@g-C_3N_4/ITO electrode served as an electro-analytical platform for constructing the immunosensor. Initially, a solution containing 0.1 M NHS, 0.4 M EDC, and 50 μg mL^{-1} of anti-IL8 in a phosphate-buffered saline (PBS) solution with a pH of 7.0 was formulated. This mixture, consisting of anti-IL8, EDC (activator), and NHS (coupling agent) in a proportion of 2 : 1 : 1, underwent incubation for 45 min before utilization. Following this, 30 μL of this solution was deposited onto the APTES@g-C_3N_4/ITO electrode within a controlled humidity environment, maintained at 25 °C, for approximately 6 hours. After incubation, the residual unbound antibodies were eliminated by rinsing the electrode with 200 μL of pH 7.0 PBS. The establishment of covalent bonds between the carboxyl group (–COOH) located on the Fc segment of the anti-IL8 and the –NH_2 moiety of the APTES molecules facilitated the immobilization of anti-IL8 molecules onto the APTES@g-C_3N_4/ITO electrode. EDC activated the –COOH groups of anti-IL8, forming an unstable *O*-acylisourea ester, which reacted with NHS to produce a stable amine-reactive NHS ester intermediate. The amino (–NH_2) groups in APTES molecules formed amide bonds with the NHS-activated anti-IL8, facilitating their covalent linkage.[46] Furthermore, 10 μL of 2% BSA was applied to the anti-IL8/APTES@g-C_3N_4/ITO immunoelectrode to block non-specific binding sites and incubated in a humid environment for 2 h. The electrode was then washed with 100 μL of PBS and stored at 4 °C for subsequent use. A schematic illustration of the sequential development of the BSA/anti-IL8/APTES@g-C_3N_4/ITO immunosensing bioelectrode for detecting IL8 in saliva samples is presented in Scheme 2.

2.5 Analyte (IL8) sample preparation

A pH 7.4 PBS solution was utilized to prepare various IL8 concentrations, which were then applied to the surface of the immunoelectrode for 9 min. The IL8 concentrations ranged from 500 fg mL^{-1} to 160 ng mL^{-1}. Subsequently, the resulting immunoreactions were evaluated using CV and DPV techniques in PBS of pH 7 containing NaCl (0.9%) and 5 mM redox couples. For DPV analysis, pulse time and pulse potential were set at 0.07 s and 0.02 V, respectively, with DPV recordings conducted at a scan rate of 0.02 V s^{-1}. Meanwhile, CV measurements were performed in a potential range of −0.8 to +0.8 V and at a scanning rate of 50 mV s^{-1}. The practical significance of the developed immunosensor was evaluated by analyzing real human samples, such as saliva, to assess its performance in real-world scenarios.

2.6 Preparation of real samples

To assess the practical applicability of the BSA/anti-IL8/APTES@g-C_3N_4/ITO immunosensor, saliva samples were utilized. A healthy volunteer provided a saliva sample for authentic sample analysis. Additionally, to evaluate the immuno-

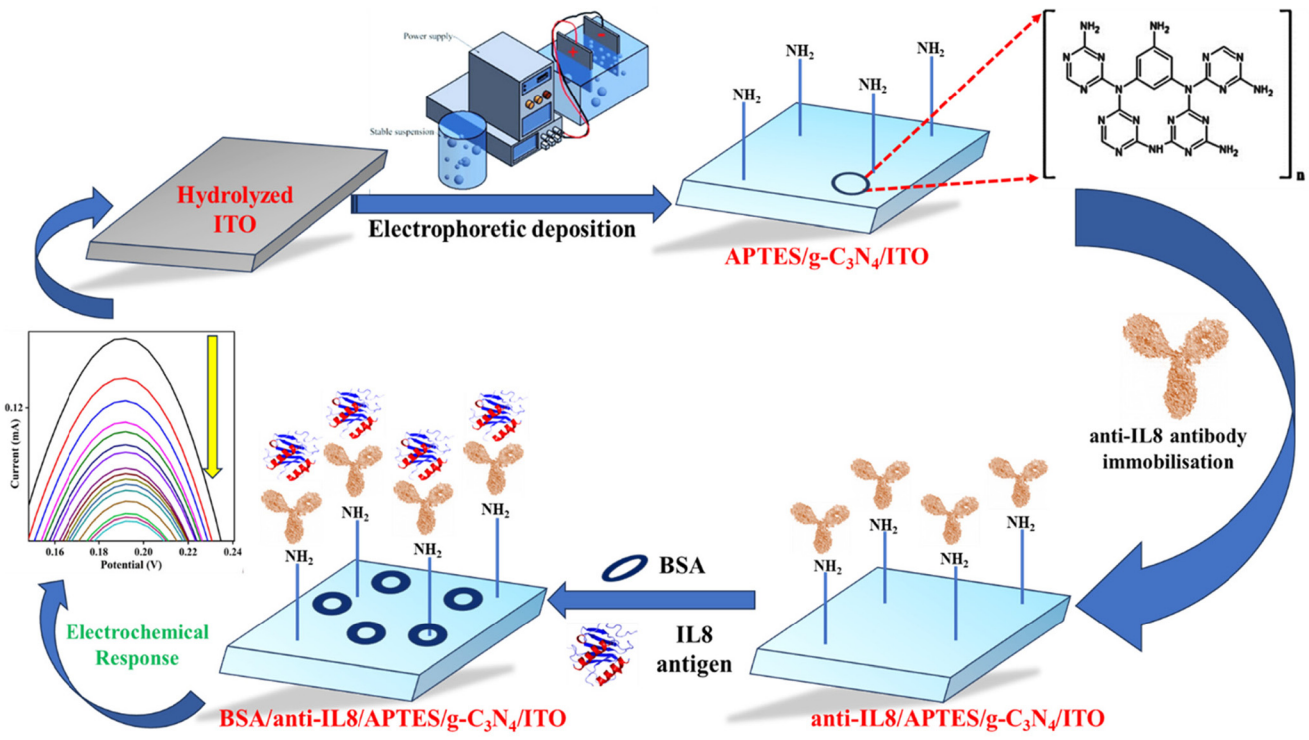

Scheme 2 An illustrative diagram outlining the sequential process of creating an immunoassay platform to detect the IL8 biomarker in saliva samples utilizing g-C_3N_4 as the foundation.

sensor's performance with real samples, IL8 was spiked into control saliva. The control saliva sample underwent centrifugation at 8000 rpm for 15 min to eliminate any particulate matter or remnants of the substance, yielding a visibly transparent supernatant. This supernatant was then spiked with various quantities of IL8, without dilution, and DPV was employed to assess the binding to BSA/anti-IL8/APTES@g-C_3N_4/ITO immunoelectrodes.

3 Results and discussion

3.1 Structural studies

The structural and compositional properties of the synthesized g-C_3N_4 generated from urea were examined using standard analytical methods. The XRD diffraction pattern is shown in Fig. 1(a), where two prominent peaks at $2\theta = 27.4°$ (002 planes) are characteristic of the g-C_3N_4 diffraction pattern. The XRD output, corresponding to a *d*-spacing of 0.367 nm, is typically used to illustrate how the π-conjugated layers are stacked.[47] Approximately at $2\theta = 13.4°$, there is another weak peak resulting from the stacking of the tri-s-triazine motif in-plane, which is associated with the (100) planes that indicate the production of g-C_3N_4.[48] The SAED pattern and HR-TEM analysis are also used to determine the planes and the *d*-spacing value of g-C_3N_4. These findings supported the *d*-spacing value of the g-C_3N_4 inter-stacking layer by the presence of a peak at 13.1° that belonged to the (100) plane, and they also matched with the XRD data. Using the Debye–Scherer formula shown in eqn (1), it was possible to determine the crystallite size of g-C_3N_4 to be around 1.28 nm, corresponding to the brightest peak (100).

$$D = \frac{k\lambda}{\beta \cos \theta} \quad (1)$$

where λ represents the wavelength of the source (1.540 Å for Cu-Kα), θ denotes the diffraction angle, β signifies the FWHM of the diffraction peak in seconds (s), D represents the crystallite size, and k stands for the crystallization constant (approximately 0.94).

FT-IR was used to characterize the chemical composition of the produced g-C_3N_4 to confirm that the compound was successfully synthesized. A transmittance mode was utilized to conduct the experiment. In the 400–4000 cm^{-1} wavelength range, a diamond crystal was present and it was scanned at 16 different resolutions of 5 cm^{-1}. The outcome is shown in Fig. 1(b). As depicted in Fig. 1(b), the molecular structure of g-C_3N_4 is illustrated through distinct infrared (IR) bands. The peak observed at 810 cm^{-1} is related to the out-of-plane twisting oscillation of the heptazine/triazine ring,[49] which confirms its existence. Moreover, the peak observed at 890 cm^{-1} corresponds to the N–H vibration's deformation mode. The stretching vibration modes of the heptazine's heterocycle ring units are observed as strong bands at 1416, 1458, 1554, and 1630 cm^{-1}.[50] Intense peaks at 1237 cm^{-1} and 1320 cm^{-1} suggest the stretching vibration of the connecting secondary amine subunits (C–NH–C). The broad weak peak at around 3000–3500 cm^{-1} can be attributed to the stretching vibration modes because of the residual/uncondensed $-NH_2$ groups' N–H or O–H bonds.[51]

3.2 Morphological studies

The composite was morphologically characterized using SEM. Before conducting the SEM, the sample was vacuum-dried and placed directly over carbon tape to produce SEM images. The SEM image of the synthesized g-C_3N_4 at 1 μm scale is depicted in Fig. 2(a), whereas the zoom version displays the SEM image at 500 nm scale. Exfoliated sheets of the synthetic material are shown in the outcome. When urea is thermally treated with a high temperature, the oxygenated precursor motif releases gases, forming g-C_3N_4. This type of morphology is quite frequent. The inset of Fig. 2(a) shows a more vivid observation of the exfoliated g-C_3N_4's pore structure under magnification. Our synthesized material shows significantly improved electrochemical performance for the IL8 sensing application, as will be demonstrated appropriately later. The exfoliated porous material naturally has higher specific capacitance characteristics, contributing to the superior electrochemical performance.

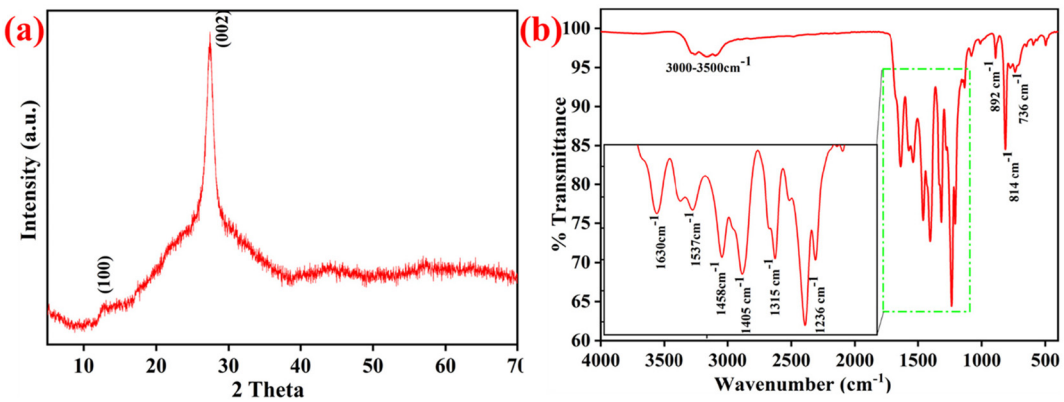

Fig. 1 (a) XRD patterns and (b) FT-IR spectra of g-C_3N_4.

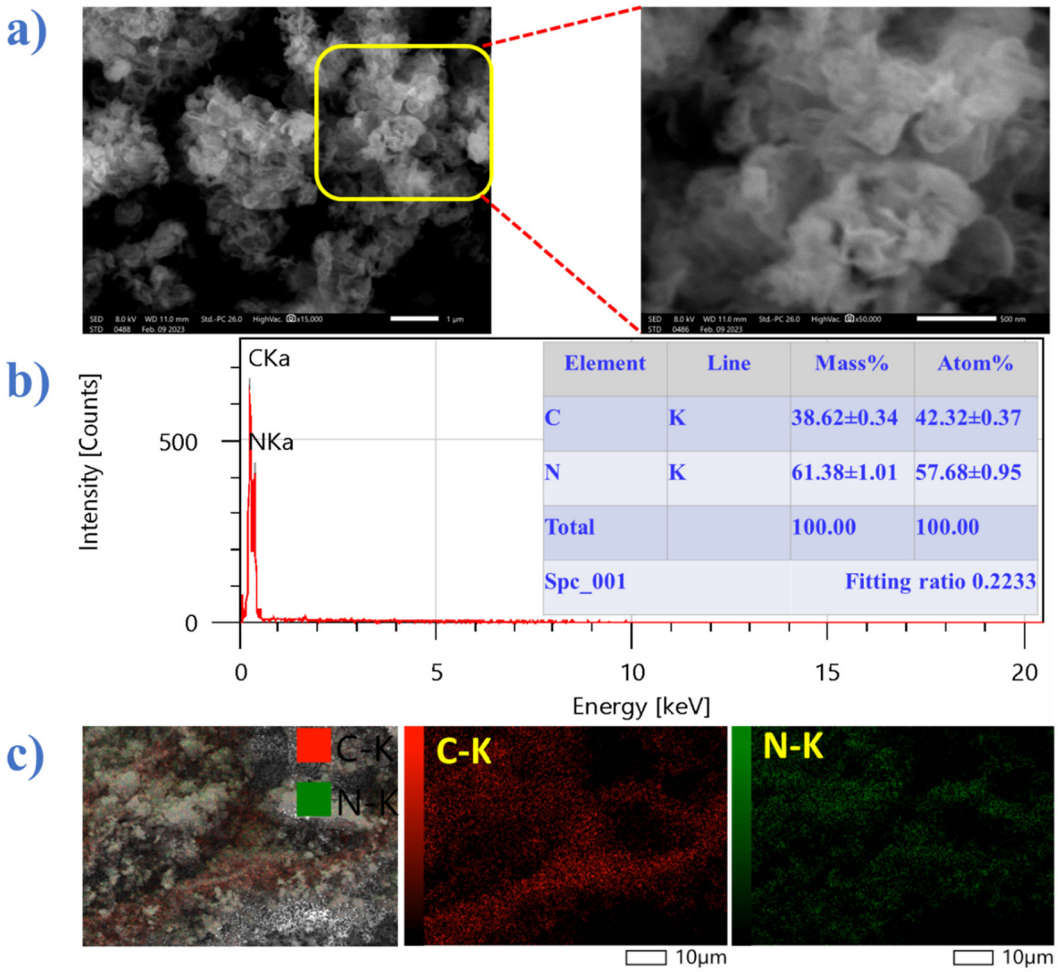

Fig. 2 (a) SEM images of g-C_3N_4 at 1 μm and 500 nm scales; (b) EDX image and (c) SEM elemental mapping of g-C_3N_4.

The uniform distribution of every element in g-C_3N_4 was then further verified by the SEM-EDS elemental mapping pictures [Fig. 2(c)]. In g-C_3N_4, the EDS examination verified the existence of the corresponding elements in terms of mass and atomic percentages [Fig. 2(b)], where the elemental amounts of carbon and nitrogen were calculated to be 38.62 ± 0.34 and 61.38 ± 0.34, respectively. Furthermore, energy-dispersive spectroscopy (EDS) was used to validate the elements C and N.

TEM and HR-TEM conducted to analyze the shape and internal framework of the produced g-C_3N_4, as shown in Fig. 3 (a–d). The morphologies of pure g-C_3N_4 at sizes of 100 nm [Fig. 3(a)] and 20 nm [Fig. 3(b)] show a structure of stacked flat sheets with wrinkles, uneven forms, and a distinctive crumpled layered structure. This structure is 2D and has a typical irregular porousness. The HR-TEM picture in Fig. 3(c) depicts the crystal structure of g-C_3N_4. The interplanar spacing between the crystal planes was measured to be 0.309 nm, precisely corresponding to the (002) planes of the corroded phase. The electron diffraction pattern of g-C_3N_4, as shown in Fig. 3(d), exhibits diffraction rings that signify the highly crystalline structure of g-C_3N_4. This discovery aligns with the findings derived from XRD.

3.3 Characterization of the modified electrodes in each step

3.3.1 SEM analysis. SEM is a powerful imaging technique that provides high-resolution images of the surface of various materials and is used in biosensors to visualize the alterations observed in the electrode surface morphology pre- and post-immobilization of biomolecules, such as antibodies and BSA. The SEM images of bare ITO electrodes at various magnifications [Fig. 4(a–c)] reveal the uniform and predominantly homogeneous surface, exhibiting a prototypical morphology commonly associated with untreated ITO. The pristine electrodes exhibit a flat, homogeneous surface and uniform appearance, reflecting the ITO material's inherent properties and providing a baseline for understanding the initial topography. Following the modification with APTES@g-C_3N_4 onto the ITO electrodes (APTES@g-C_3N_4/ITO), SEM analysis showed discernible alterations in the surface morphology. The exfoliated sheet-like structure of g-C_3N_4 manifests as interconnected thin layers covering the ITO surface. These sheets appeared as a network of 2D structures resembling a graphene-like lattice. The images also showed attachment points, edges, and potential interactions between the modified layer and the underlying

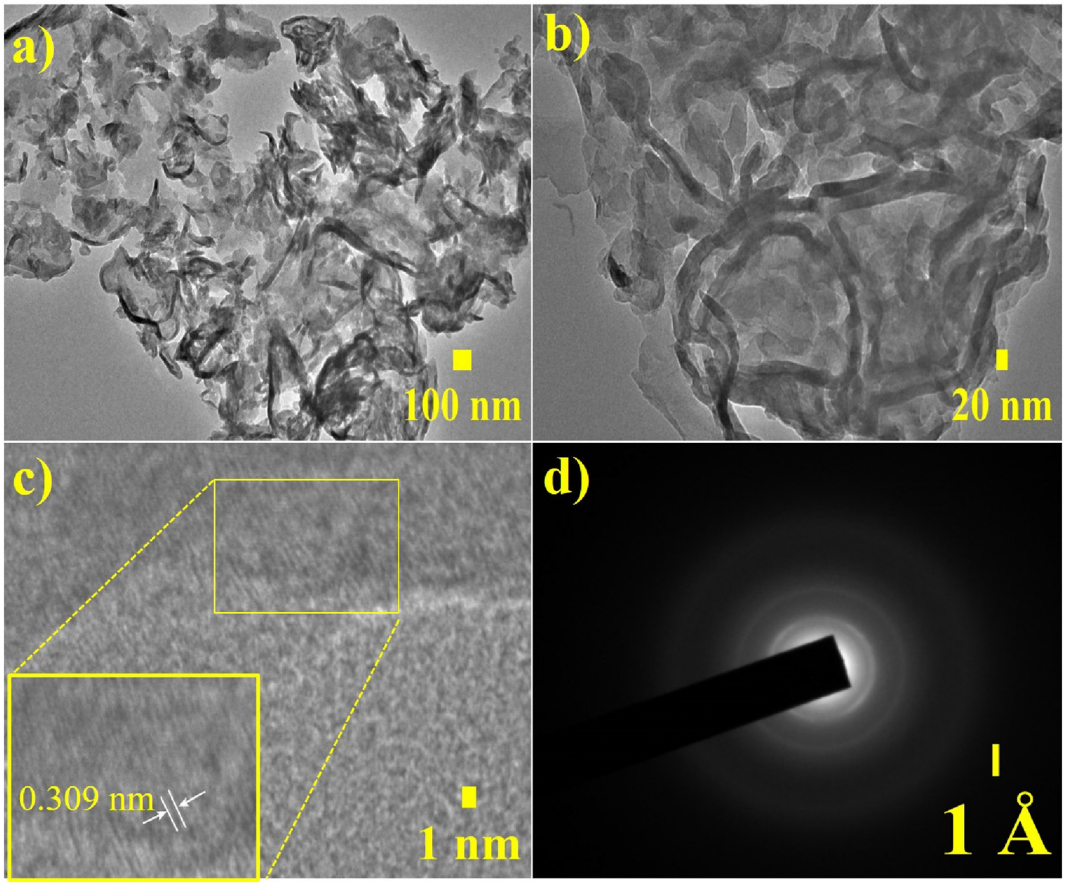

Fig. 3 TEM images of the synthesized g-C_3N_4 at lower (a) and higher magnifications (b); HR-TEM image (c) and SAED pattern (d) of g-C_3N_4.

electrode material, as shown in Fig. 4(d–f). Following the immobilization of anti-IL8 antibodies onto the g-C_3N_4-modified ITO electrodes (anti-IL8/APTES@g-C_3N_4/ITO), SEM imaging reveals the existence of anomalous morphological configurations and agglomerates suggestive of the anchoring of antibodies [Fig. 4(g–i)]. These large biomolecules with their distinct 3-D shapes left an imprint on the electrode's surface, leading to visible changes in topography. This can be observed as surface roughness or irregularities, indicating the effective binding of antibodies. The subsequent step involves the attachment of BSA onto the modified electrodes (BSA/anti-IL8/APTES@g-C_3N_4/ITO). SEM images illustrate a further alteration in the structure. Unlike antibodies, BSA molecules are smaller, leading to a more uniform and homogeneous coverage on the electrode's surface, as depicted in Fig. 4(j–l). This yields a comparably uniform and uninterrupted coating juxtaposed with irregular aggregates precipitated by the antibodies.

3.3.2 Contact angle (CA) analysis. At each step of the biosensor development process, the hydrophobic/hydrophilic properties of the modified electrodes were evaluated using CA experiments by the sessile drop method [Fig. 4(m–p)]. For the unaltered hydrolyzed ITO electrode [Fig. 4(m)], the CA of 82.9° suggested a slightly hydrophobic character. The CA dramatically decreased to 31.9° [Fig. 4(n)] after the EPD of APTES@g-C_3N_4 onto the ITO electrode, indicating an exceptional hydrophilic property of the APTES@g-C_3N_4/ITO electrode. Following immobilizing the BSA molecule and anti-IL8 on the APTES@g-C_3N_4/ITO electrode, the CA decreased to 0° [Fig. 4(o and p)], demonstrating the hydrophilic nature of the material. This increased hydrophilicity helps anti-IL8 adhere to an aqueous PBS buffer, increasing the sensitivity of the biosensor created to detect IL8 biomarkers in saliva samples.[52]

3.3.3 FT-IR analysis. The FT-IR spectra provide valuable insights into the chemical composition and structural changes of the modified electrodes at different stages of functionalization. In the FT-IR spectrum of APTES@g-C_3N_4/ITO [Fig. S1(a)†], characteristic peaks are observed at 1000–1200 cm^{-1} associated with silane modification, indicative of Si–O–Si stretching vibrations from the APTES molecule. The presence of g-C_3N_4 was discerned through specific peaks, as explained above [Fig. 1(b)], corresponding to the nitrogen-containing functional groups.

Furthermore, upon immobilizing anti-IL8 onto the APTES@g-C_3N_4/ITO electrode, notable changes in the FT-IR spectrum were seen, as depicted in Fig. S1(b).† The spectrum exhibited distinctive peaks of amide bonds, specifically in the amide I (2137 cm^{-1}) and amide II (2481 cm^{-1}) regions, signifying

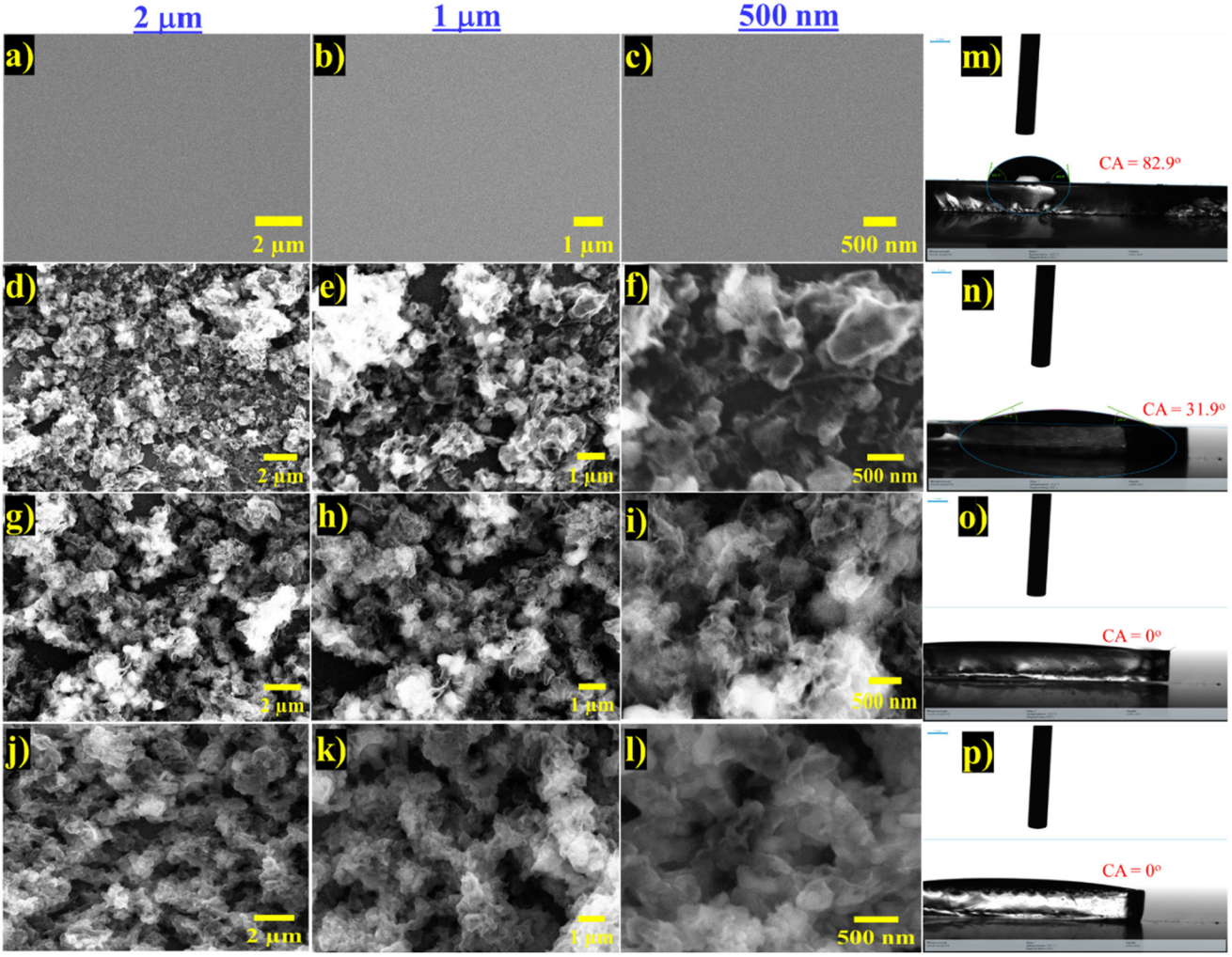

Fig. 4 SEM images at 3 different scales, *i.e.*, 2 μm, 1 μm, and 500 nm of each modified electrode: (a–c) ITO, (d–f) APTES@g-C_3N_4/ITO, (g–i) anti-IL8/APTES@g-C_3N_4/ITO, and (j–l) BSA/anti-IL8/APTES@g-C_3N_4/ITO; contact angle studies of (m) ITO, (n) APTES@g-C_3N_4/ITO, (o) anti-IL8/APTES@g-C_3N_4/ITO, and (p) BSA/anti-IL8/APTES@g-C_3N_4/ITO.

the successful attachment of anti-IL8. These amide bands indicate the anti-IL8 proteinaceous nature and confirm their presence on the modified surface.[53] After the subsequent immobilization of BSA, additional changes in the FT-IR spectrum were observed, as shown in Fig. S1(c).† The manifestation or augmentation of prominent peaks within the pertinent regions confirmed the efficacious immobilization of BSA molecules onto the anti-IL8/APTES@g-C_3N_4/ITO electrode surface.

3.4 Electrochemical studies

Electrochemical investigations were conducted using a three-electrode setup, which included an Ag/AgCl reference electrode (RE), a platinum auxiliary/counter electrode (CE), and an ITO-coated glass substrate as the working electrode (WE). Utilizing CV, the electrochemical characteristics of the APTES@g-C_3N_4-modified ITOs with $[Fe(CN)_6]^{3-/4-}$were investigated. Though the kinetics and slopes varied, the CVs of each electrode revealed a typical Fe^{2+}/Fe^{3+} redox pair. The oxidation process (Fe^{2+} to Fe^{3+}) has a substantially lower slope than the reduction process (Fe^{3+} to Fe^{2+}), indicating that the APTES@g-C_3N_4 nanomaterials are causing a shift away from reversibility. Thus, the reduction process can happen comparatively faster than the oxidation process due to the interfaces changed by APTES@g-C_3N_4 nanomaterials. This might result from the carbon nitride components acting more like reducing agents. Because nitrogen lone pairs and oxygen functional groups are present, their surfaces typically have surplus negative charges that favor the reduction reaction over the oxidation events.

3.4.1 Optimization of experimental conditions. Enhancing the diverse experimental parameters for optimization is crucial for creating a biosensor that is sensitive, repeatable, and reproducible. We fine-tuned various experimental conditions such as investigating the ideal parameters for EPD, including voltage and duration, as the first step. Other factors to consider include the concentration of anti-IL8, the duration of the anti-IL8 incubation period, the concentration of BSA, the interaction time for the antigen (response time), and the impact of the redox couple $[Fe(CN)_6]^{3-/4-}$ prior to immunosensor characterization and perform-

ance evaluation in determining the optimal experimental conditions. ESI Section S3† comprehensively describes every optimized parameter, which is also graphically displayed in Fig. S2 (a–f).† Table S2† provides the optimized values for each experimental parameter (tried *vs.* selected).

3.4.2. Effect of scan rate studies. The scan rate of any electrochemical biosensor strongly influences the electrocatalytic behavior of the prepared electrodes. To comprehend the electro-oxidation of IL8, CVs were examined using APTES@g-C_3N_4/ITO and BSA/anti-IL8/APTES@g-C_3N_4/ITO electrodes by progressively increasing the scan rate from 10–100 mV s^{-1}, as shown in Fig. 5(A) and (B), respectively. In both scenarios, the anodic peak potentials gradually moved to the positive side, most likely due to mass transfer and kinetic constraint. The potential peak shifts to the positive side and IL8 oxidation at the APTES@g-C_3N_4/ITO electrode and the BSA/anti-IL8/APTES@g-C_3N_4/ITO immunoelectrode surface is an irreversible reaction governed by a diffusion mechanism, as indicated by the anodic peak current fluctuating linearly with the square root of the scan rate.[54] Furthermore, the electron transfer kinetics of the electrode became quasi-reversible as scan speeds increased due to the electrode's peak-to-peak separation potential increasing and passing through the higher potential end. This is a result of the fact that diffusion species have less time to reach the electrode surface as the scan rate increases. This leads to a wider separation between the reduction and oxidation peaks as the reduction and oxidation processes become more kinetically regulated. Therefore, maintaining a suitable peak separation and getting a better current response may have to be traded off when the scan rate increases.

Fig. 5A(i) and B(i) show the linear range between the oxidation peak current (I_{pa}) and the reduction peak current (I_{pc}) *vs.* square of the scan rate (mV s^{-1}) and follow eqn (2)–(5):

$$\mathrm{IPa(APTES@g\text{-}C_3N_4/ITO)} = [0.025\ \mathrm{mA} \times (\text{scan rate}\ [\mathrm{mV\ s^{-1}}])^{1/2}] + 0.085\ \mathrm{mA};\quad R^2 = 0.994 \tag{2}$$

$$\mathrm{IPc\ (APTES@g\text{-}C_3N_4/ITO)} = -[0.039\ \mathrm{mA} \times (\text{scan rate}[\mathrm{mV\ s^{-1}}])^{1/2}] + 0.072\ \mathrm{mA};\quad R^2 = 0.994 \tag{3}$$

$$\mathrm{IPa(BSA/anti\text{-}IL8/APTES@g\text{-}C_3N_4/ITO)} = [0.04\ \mathrm{mA} \times (\text{scan rate}\ [\mathrm{mV\ s^{-1}}])^{1/2}] + 0.006\ \mathrm{mA};\quad R^2 = 0.995 \tag{4}$$

$$\mathrm{IPc(BSA/anti\text{-}IL8/APTES@g\text{-}C_3N_4/ITO)} = -[0.03\ \mathrm{mA} \times (\text{scan rate}\ [\mathrm{mV\ s^{-1}}])^{1/2}] + 0.006\ \mathrm{mA};\quad R^2 = 0.993 \tag{5}$$

Additionally, Fig. 5A(ii) and B(ii) demonstrate that the peak-to-peak spacing shifted with increasing scan rate, suggesting that the process is electrochemically quasi-reversible. It was observed that the anodic and cathodic peak currents moved toward the higher and lower potentials, respectively, as the scan rate increased. The anodic and cathodic peak potentials, E_{pa} and E_{pc}, respectively, have a linear relationship with the square root of scan rate ($\Delta E = E_{pa} - E_{pc}$); this suggests that the kinetics of charge transfer between the electrode and the electrolyte are amicable, as stated in eqn (6) and (7). Analysis of

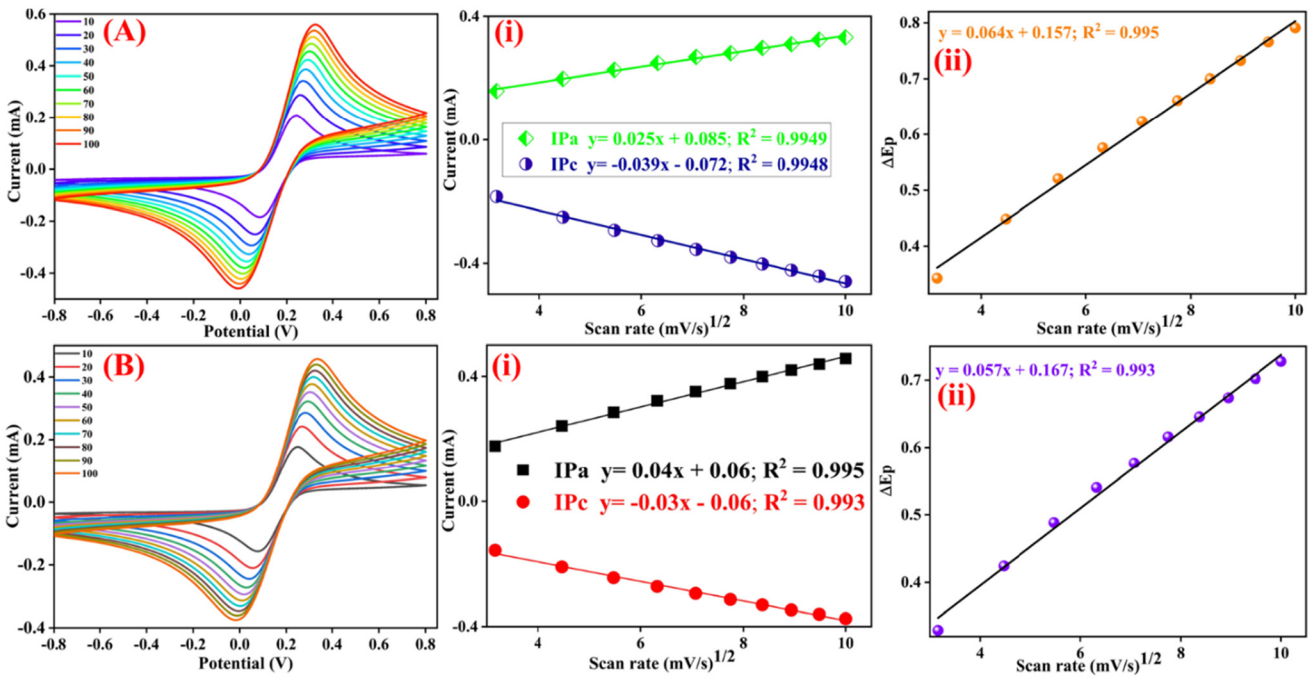

Fig. 5 CV profiles of (A) the APTES@g-C_3N_4/ITO electrode and (B) the BSA/anti-IL8/APTES/g-C_3N_4/ITO immunoelectrode. (A(i)) and (B(i)) display the oxidation and reduction peak currents normalized to the square root of the scan rate, while (A(ii)) and (B(ii)) demonstrate the divergence observed in cathodic and anodic peak potentials (ΔE_p) in relation to the square root of the scan rate.

the scan rates for both the APTES@g-C_3N_4/ITO electrode and the BSA/anti-IL8/APTES@g-C_3N_4/ITO immunoelectrode reveals a shift of the reduction current peak towards the negative potential and the oxidation current peak towards the positive potential. Additionally, an increase in scan rate leads to a rise in peak potential (E_{pa} and E_{pc}), indicating a sluggish flow of electrons across the interface.

$$\Delta E_P(\text{APTES@g-C}_3\text{N}_4/\text{ITO}) = [0.064\,\text{V} \times (\text{scan rate}\,[\text{mV s}^{-1}])^{1/2}] + 0.157\,\text{V};\quad R^2 = 0.995 \tag{6}$$

$$\Delta E_P(\text{APTES@g-C}_3\text{N}_4/\text{ITO}) = [0.057\,\text{V} \times (\text{scan rate}\,[\text{mV s}^{-1}])^{1/2}] + 0.167\,\text{V};\quad R^2 = 0.993 \tag{7}$$

The kinetic interface properties of the BSA/anti-IL8/APTES/g-C_3N_4/ITO and APTES@g-C_3N_4/ITO electrodes were evaluated to investigate electron dynamics (the detailed explanation of each parameter is provided in ESI S4†). Table 1 presents the calculated values of various electrochemical parameters for the respective electrodes' ionic species encompassing the cathodic peak current (I_{pc}), diffusion coefficient (D), anodic peak current (I_{pa}), average surface concentration (γ^*), charge transfer rate constant (K_s), and electroactive surface area (A_e). In Table 1, we have compared the diffusion coefficient (D) values for APTES/g-C_3N_4/ITO electrode and BSA/anti-IL8/APTES/g-C_3N_4/ITO immunoelectrode. From the Table, it has been observed that the lower D values for the BSA/anti-IL8/APTES@g-C_3N_4/ITO immunoelectrode, compared to APTES@g-C_3N_4/ITO electrode, indicate that the added biomolecule layers, such as BSA and anti-IL8 antibodies, act as barriers, reducing electron transfer and blocking electroactive species from accessing the electrode surface. The immobilization of these high molecular weight, non-conductive biomolecules decreases charge transfer and creates steric hindrance, leading to slower diffusion and electron kinetics, which further obstruct the movement of electroactive species toward the surface. These combined factors contribute to the lower D value observed in the BSA/anti-IL8/APTES/g-C_3N_4/ITO immunoelectrode due to the BSA and anti-IL8 biomolecules.

3.4.2. pH studies. The pH studies were conducted to find the ideal pH of PBS buffer for the BSA/anti-IL8/APTES@g-C_3N_4/ITO immunoelectrode. PBS containing redox species was utilized for this investigation, with a scan rate of 50 mV s^{-1}. The electrochemical reactivity of the BSA/anti-IL8/APTES@g-C_3N_4/ITO immunoelectrode was assessed in correlation with pH variations (ranging from 6.0 to 8.0) using CV and DPV methods. The results depicted in Fig. 6(a) and 7(b) reveal a direct correlation between the charge on proteinaceous biomolecules and the pH of the buffer solution in which they are dissolved, thereby influencing the electrochemical response.[55] Furthermore, the maximum anodic current was found at pH 7.0 according to a graph showing the peak current (oxidation) as a function of pH [inset of Fig. 6(a) and (b)]. This finding implies that the proteinaceous biomolecule, or antibody, exists in its natural state at neutral pH and has great stability and activity.

On the other hand, when H^+ or OH^- ions interact with the antibodies' amino acids, these materials tend to denature in acidic or basic pH ranges. Although biomolecules are often thought to respond with a high current at their isoelectric point (pI), the electrochemical reaction is negatively impacted at a modest pI.[56] In light of this, additional electrochemical investigations were conducted utilizing PBS under neutral pH conditions (pH 7.0).

3.4.3. Electrochemical studies of fabricated electrodes. Electrochemical DPV and CV in PBS solutions (pH 7.0) containing $[Fe(CN)_6]^{3-/4-}$ were used to investigate the electron transport characteristics of different g-C_3N_4-based modified electrodes. The CV results for several immunoelectrodes are shown in Fig. 7(c). The immunoelectrodes tested include bare ITO, APTES@g-C_3N_4/ITO, anti-IL8/APTES@g-C_3N_4/ITO, and BSA/anti-IL8/APTES@g-C_3N_4/ITO. The CV measurements were performed in a potential range of −0.8 V to +0.8 V, with a scan rate of 50 mV s^{-1}. The peak separation, exceeding 400 mV for hydrolyzed unmodified ITO, is affected by several parameters. The small peak current value of CV for the unmodified ITO electrode [0.407 mA (curve i)] suggests a quasi-reversible electrochemical mechanism and delayed electron transport on the ITO electrode.

Conversely, following the EPD of APTES@g-C_3N_4 on ITO, the peak current in the APTES@g-C_3N_4/ITO electrode increased dramatically to 0.425 mA (curve ii), indicating a rapid electron transfer between the electrolyte interface and APTES@g-C_3N_4/ITO. Apart from the improvement of the electron transfer process following the deposition of APTES@g-C_3N_4 onto the bare ITO surface (discussion above), it is clear that the immobilization of the anti-IL8 antibodies and the subsequent formation of the complex with IL8 caused the overall electrode process to deteriorate. The peak current falls (about from 0.425 mA to 0.408 mA) and the ΔE_p rises (roughly from 0.088 to 0.388 V) in accordance. When large molecules, additional antibodies, or aptamers are immobilized on an electrode surface, the effects are comparable to those documented in the literature. BSA served as a blocking reagent to hinder non-specific binding events occurring at the anti-IL8/APTES@g-C_3N_4/ITO electrode interface. The inherent insula-

Table 1 Predicted values of electrochemical parameters for electrodes

Electrode	D (cm^2 s^{-1})	A_e (mm^2)	γ^* (mol cm^2)	K_s (s^{-1})	I_{pa} (A)	I_{pc} (A)
APTES@g-C_3N_4/ITO	31.95×10^{-12}	0.329	3.64×10^{-8}	0.299	4.25×10^{-4}	3.54×10^{-4}
BSA/anti-IL8/APTES@g-C_3N_4/ITO	19.73×10^{-12}	0.670	2.86×10^{-8}	0.197	3.34×10^{-4}	2.94×10^{-4}

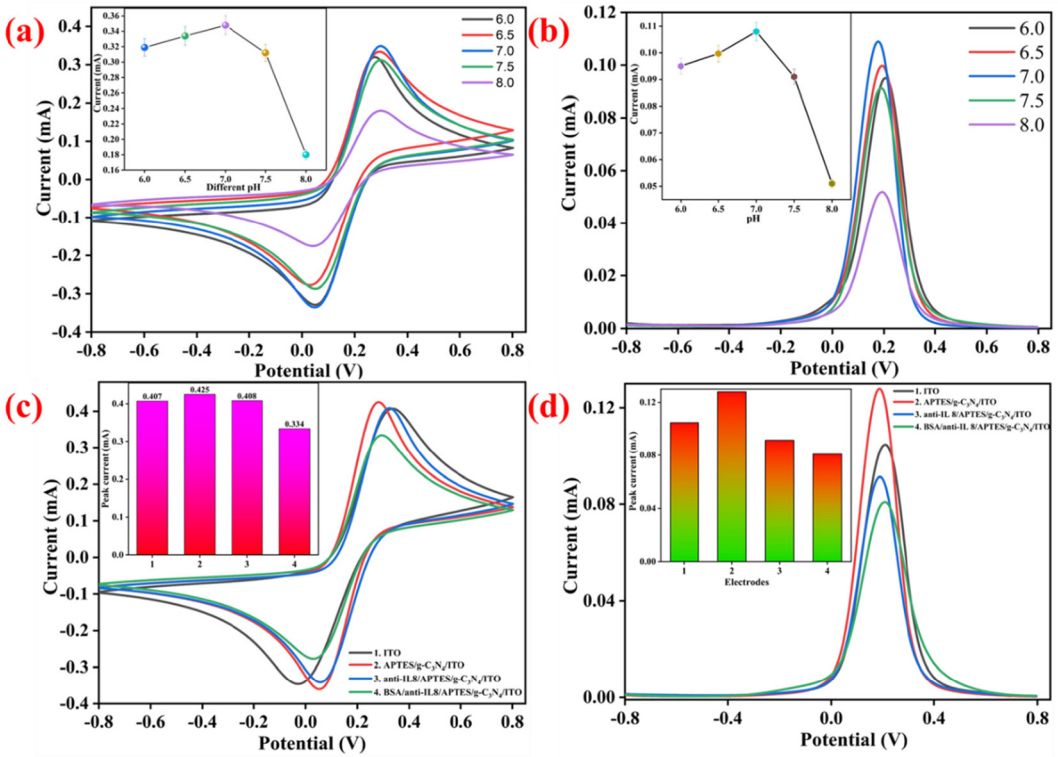

Fig. 6 pH study using (a) CV and (b) DPV techniques (the line plot demonstrating the correlation between the pH and the peak current (oxidation) can be found in the inset images); (c) CV and (d) DPV curves of various modified electrodes (the bar plot between the peak current and various modified electrodes is displayed in the inset). Three distinct experiments were conducted to acquire the error bars.

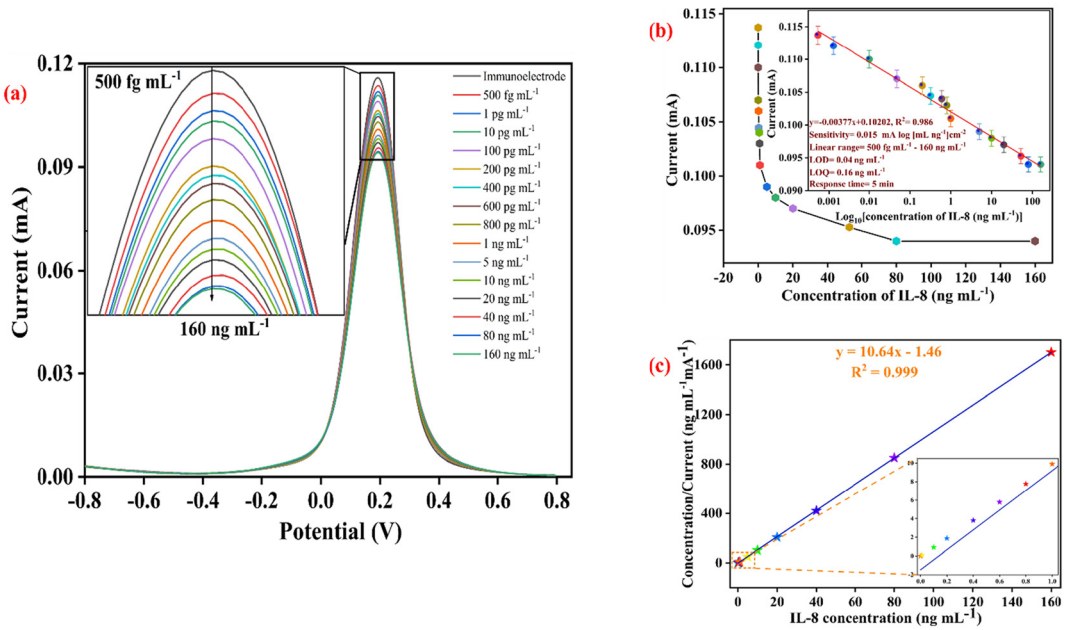

Fig. 7 (a) Illustration of the electrochemical response of the sensing platform towards IL8 concentrations using DPV (the enlarged view is displayed in the inset); (b) a calibration plot obtained using DPV techniques between the anodic peak current magnitude and the $\log_{10}$ of the IL8 concentration; and (c) Hanes–Wolf plot. Three separate tests were conducted to acquire the error bars.

tive characteristics exhibited by BSA molecules, coupled with their non-specific adhesion to the accessible surface of APTES@g-C_3N_4, lead to an additional decrease in peak current upon BSA attachment, amounting to 0.334 mA (curve iv). Furthermore, DPV was performed at a scan rate of 50 mV s^{-1} for bare ITO and the APTES@g-C_3N_4/ITO, anti-IL8/APTES@g-C_3N_4/ITO, and BSA/anti-IL8/APTES@g-C_3N_4/ITO immunoelectrodes within the potential range of −0.8 to +0.8 V. The obtained results were comparable to the CV findings illustrated in Fig. 6(d).

The electron transfer abilities of bare ITO, APTES@g-C_3N_4/ITO, anti-IL8/APTES@g-C_3N_4/ITO, and BSA/anti-IL8/APTES@g-C_3N_4/ITO were also investigated in 0.2 M PBS containing 5 mM $[Fe(CN)_6]^{3-/4-}$ in the potential between −0.8 and +0.8 V vs Ag/AgCl using CV at a scan rate of 50 mV s^{-1} [Fig. 6(c)]. Table 2 compares the measured oxidation and reduction peak current densities (J_{pa} and J_{pc}), anodic and cathodic peak potentials (E_{pa} and E_{pc}), and potential differences (ΔE_p). Consequently, compared to other modified and bare ITO electrodes, the BSA/anti-IL8/APTES@g-C_3N_4/ITO electrode showed lower ΔE_p and more significant redox peak currents (Table 2). This could be because of the APTES@g-C_3N_4 surface's favorable electrostatic interactions with $[Fe(CN)_6]^{3-/4-}$ ions.

3.4.4. Analytical performance of the proposed biosensor for IL8 detection. The response time study performed before conducting the electrochemical response investigations of the biosensing electrode [Fig. S4(f)†]. The objective was to ascertain the incubation duration necessary for the IL8 to interact with the BSA/anti-IL8/APTES@g-C_3N_4/ITO immunoelectrode. We determined that 15 minutes was the ideal duration for the proper binding between the IL8 and the BSA/anti-IL8/APTES@g-C_3N_4/ITO electrode. We monitored the results at regular intervals of 2 min for a maximum of 20 min. Therefore, to facilitate subsequent electrochemical studies, 15 min of incubation time optimized prior to each electrochemical measurement.

We tested whether the BSA/anti-IL8/APTES@g-C_3N_4/ITO electrode could detect IL8 and comparable sensors using DPV. By removing non-faradaic currents in CV, DPV enables better sensitivity. Due to its sensitivity and selectivity, the DPV approach was used to quantitatively assess IL8 utilizing BSA/anti-IL8/APTES@g-C_3N_4/ITO. With a potential range of −0.8 V to +0.8 V and a scan rate of 50 mV s^{-1}, the developed biosensor's electrochemical response was studied in terms of IL8 antigen concentrations spanning from 500 fg mL^{-1} to 160 ng mL^{-1} for a duration of 15 min at each concentration in 0.2 M PBS containing 5 mM redox species [Fig. 7(a)]. As shown in Fig. 7(a), the DPV's current decreased as the IL8 concentration was increased from 500 fg mL^{-1} to 160 ng mL^{-1}. It is caused by increased complex formation between anti-IL8 and IL8, which prevents electron transport. Furthermore, as the IL8 concentration increased on the APTES@g-C_3N_4-modified ITO electrode surface, a greater electrically insulating layer was created on the BSA/anti-IL8/APTES@g-C_3N_4/ITO electrode, limiting the electron transfer between the immunoelectrode and $[Fe(CN)_6]^{3-/4-}$.[57] Following the completion of the IL8 binding, the current value decreases, indicating that IL8 has successfully bound to the immunosensor. A triplicate measurement was performed on the sensor. An enhanced image of the electrochemical performance is shown in the inset.

As depicted in Fig. 7(b), under optimal conditions for the assay, the current value (ΔI) variation displayed a highly linear correlation with IL8 concentrations spanning from 500 fg mL^{-1} to 160 ng mL^{-1}. Beyond this range, the current stabilizes with the addition of higher concentrations. Eqn (8) yields a linear regression coefficient (R^2) of 0.986, affirming this relationship.

$$I_P = [0.003\ (\text{mA mL ng}^{-1})] \times \log 10\ [\text{concentration of IL-8}\ (\text{ng mL}^{-1})] + 0.102; \quad R^2 = 0.986 \tag{8}$$

Using both the gradient of the calibration plot and the surface area of the immunoelectrode (0.25 cm^2), the sensitivity of the resultant immunosensor was determined to be [0.015 mA log (mL ng^{-1}) cm^{-2}], exhibiting an R^2 value of 0.986. Utilizing this remarkable LOD, the biosensor shown its capability to identify an extremely low concentration of IL8, as supported by the computations outlined in the ESI (Section S4).† This sensitivity enabled the detection of mere ~6.0×10^{-3} molecules of IL8. The computed LOD and LOQ values were 0.04 ng mL^{-1} and 0.16 ng mL^{-1}, respectively, indicating that they fall within the clinically significant range. Between 0 and 250 pg mL^{-1} is the range for healthy salivary levels of IL8; 250 to 500 pg mL^{-1} indicates an early-stage OC and 750 pg mL^{-1} indicates OC.

$$\text{LOD} = 3 \times \text{SD/slope} = 3 \times \frac{\text{SD}}{\left(\frac{dy}{dx}\right)} = 3 \times \frac{\text{SD}}{\left[\frac{dy}{d\ln x} \times \frac{d\ln x}{dx}\right]}$$
$$= 3 \times \frac{\text{SD} \times (2.303x)}{\left[\frac{dy}{d\ \log\ x}\right]} = 3 \times \frac{\text{SD} \times (2.303x)}{\text{slope of semi log plot}} w$$

where x represents the nadir of measured concentrations or the LOQ, while SD denotes the standard deviation pertaining to the intercept.

Table 2 CV profiles of various modified electrodes and their potentials and current values in 0.2 M PBS containing redox species

S. No.	Modified electrodes	E_{pa} (V)	E_{pc} (V)	J_{pa} (mA cm^{-2})	J_{pc} (mA cm^{-2})	ΔE_p (mV)
1	Bare ITO	0.335	0.127	−1.147	1.101	208
2	APTES@g-C_3N_4/ITO	0.286	0.131	−1.169	1.188	155
3	Anti-IL8/APTES@g-C_3N_4/ITO	0.308	0.173	−1.321	1.286	135
4	BSA/anti-IL8/APTES@g-C_3N_4/ITO	0.256	0.154	−1.534	1.151	102

Table 3 Matrix systems and response techniques employed in previously documented biosensors for oral cancer

S. No	Biosensing platform	Technique	Linear range	LOD	Sensitivity	Response time (min)
1	Anti-IL6/SWNTs/graphite	Amperometry	0.08–8.0 fM	0.02 fM	—	58
2	Anti-IL8/AuNPs-rGO/ITO	DPV	500 fg mL^{-1} to 50 ng mL^{-1}	72.73 pg mL^{-1}	—	59
3	Anti-IL8 IgG1 MAB208/CM5 sensor chip	SPR	9.5–191 pM	2.5 pM in buffer and 184 pM in saliva	—	60
4	Magnetic beads/screen printed electrodes	Amperometry	1–1000 fg mL^{-1}	72.4 pg mL^{-1}	—	61
5	BSA/anti-IL8/APTES@g-C_3N_4/ITO	DPV	500 fg mL^{-1} to 160 ng mL^{-1}	0.04 ng mL^{-1} (in buffer)	0.015 mA $\log_{10}$ [ng mL^{-1}] cm^{-2}	**Present work**
			500 fg mL^{-1} to 160 ng mL^{-1}	0.05 ng mL^{-1} (in saliva)	0.012 mA $\log_{10}$ [ng mL^{-1}] cm^{-2}	

Table 3 shows that the manufactured BSA/anti-IL8/APTES/g-C_3N_4/ITO immunosensor performed analytically either better or similarly to existing biosensors in terms of its primary analytical parameters, such as the linear detection range, sensitivity, and the detection limit. The LOD is strikingly much lower than any of the methods described, indicating a possible role for APTES/g-C_3N_4 in the diagnosis of OC. The particular interaction between the IL8 and anti-IL8 may cause a high sensitivity of the constructed biosensor, as it forms a well-ordered APTES@g-C_3N_4 nanomaterial. Through solid covalent interactions, this APTES@g-C_3N_4 provided a suitable matrix to bind with anti-IL8 effectively and form an established amide bond. Additionally, the created immunosensor has an enormous surface area that enables the incorporation of supplementary bio-recognition elements, facilitating an extensive linear dynamic range. The primary benefits of APTES@g-C_3N_4-based biosensors are their high-quality 3D porous surfaces, ease of mass production, and disposable nature.

Plotting the Hanes–Wolf graph between the IL8 concentration and the current of BSA/anti-IL8/APTES@g-C_3N_4/ITO immunoelectrode/IL8 concentration yields the association constant (K_a), which is 0.094 ng mL^{-1}, as shown in Fig. 7(c). The value of K_a is reliant upon multiple factors inside the intended immunosensor, such as the biomolecule attachment sites and how antibodies bind to the electrode surface, resulting in varying conformational variations within the antibody structure. The structural arrangement of anti-IL8 and greater concentration on the electrode surface are accountable for the increase in K_a value, indicating a strong binding affinity of the BSA/anti-IL8/APTES@g-C_3N_4/ITO immunoelectrode against IL8. According to estimates, the dissociation constant (K_d) value is −0.1374 ng mL^{-1}, suggesting a specific affinity for IL8. The Hanes–Wolf linear plots, derived from the inverse of the slope, have been used to evaluate the value of K_a, while the (K_d) value is the result of multiple of intercepts value and K_a.

3.4.5. Control, interferent, reproducibility, and repeatability studies. As shown in [Fig. 8(a)], a control experiment was carried out to evaluate the electrochemical current response of the APTES@g-C_3N_4/ITO electrode when exposed to different concentrations of IL8. Except for immobilizing monoclonal anti-IL8, all the experimental settings were kept the same as those used in electrochemical response tests for the BSA/anti-IL8/APTES@g-C_3N_4/ITO immunoelectrode. The outcomes showed that even at increased IL8 concentrations, the APTES@g-C_3N_4/ITO electrode maintained a constant DPV current. The absence of current variation indicates that there is no interaction between the APTES@g-C_3N_4/ITO electrode and IL8, leading to an unchanged electrochemical response. Consequently, any current variations observed in the response studies are mainly ascribed to the interplay between the IL8 and the anti-IL8 in contrast to being individually affected by the APTES@g-C_3N_4/ITO electrode.

The most essential characteristic of a biosensor is its specificity. In real life, different biological species co-exist, and it was investigated whether the sensing platform affected IL8 sensing by looking at the effects of the interaction caused by the electrochemical activities of the proposed biosensor signal. Therefore, exposure to alternative cancer biomarkers like CYFRA-21-1, p53, and SP17, as well as other salivary components like ascorbic acid, oxalic acid, glucose, urea, and uric acid, was part of the inquiry into the specificity of the manufactured immunosensor for OC. These interferants were used at a concentration of 1 ng mL^{-1} for binding with BSA/anti-IL8/APTES@g-C_3N_4/ITO. The quantification of their detection was achieved through the use of DPV, as illustrated in Fig. 8(b). Comparing the immunosensor to the other biomarkers, the immunosensor showed noticeably higher specificity for IL8. Interestingly, including the biochemicals mentioned above did not affect the anodic peak current of the proposed immunosensor. It appears from this result that the influence of interfering drugs was minimal. The reason behind the acceleration of the particular interaction towards IL8 could be the specific interaction between the IL8 and anti-IL8 molecules on the surface of BSA/anti-IL8/APTES@g-C_3N_4/ITO.

The practical implementation of immunosensors requires certain important properties, namely reproducibility and repeatability. The repeatability of the BSA/anti-IL8/APTES@g-C_3N_4/ITO immunoelectrode was evaluated using six distinct immunoelectrodes that were prepared under comparable experimental settings and used individually for each experiment,[62] as shown in [Fig. 8(c)]. Likewise, repeatability studies were conducted utilizing the same DPV methodology to get six consecutive measurements for a particular concen-

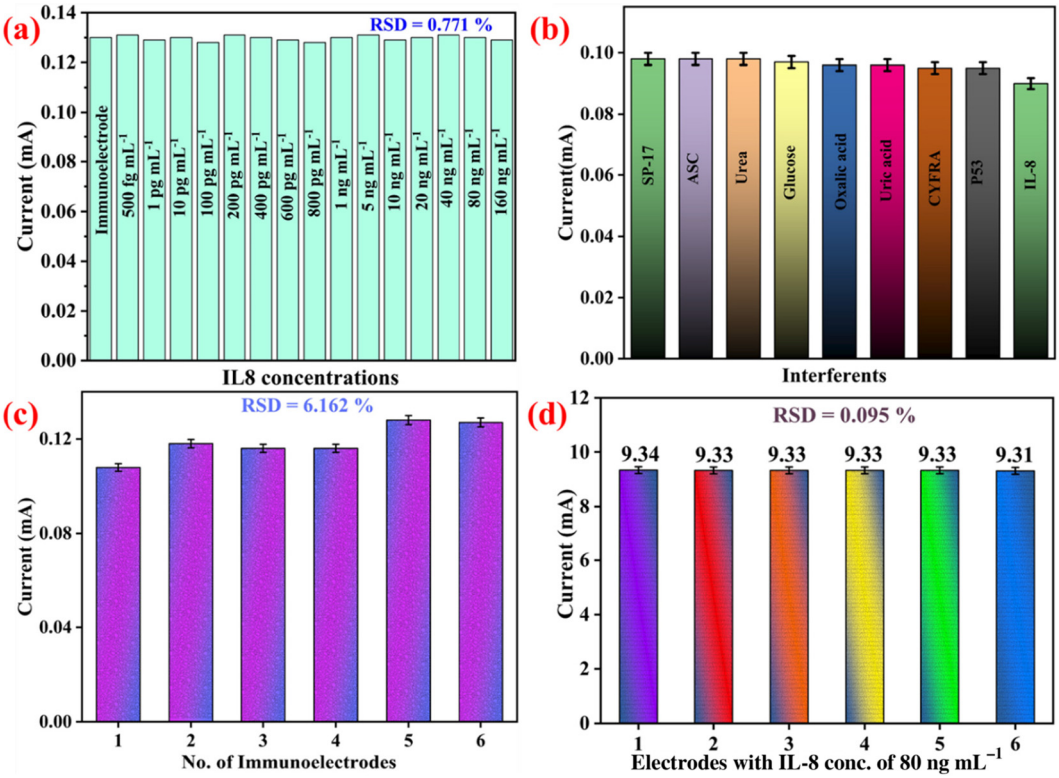

Fig. 8 (a) Control study; (b) interferent (specificity) study; (c) reproducibility study of six different fabricated immunoelectrodes; and (d) repeatability study. The error bars represent the results derived from three separate and independent experiments.

tration of IL8 (80 ng mL^{-1}), as illustrated in [Fig. 8(d)]. Reproducibility and repeatability were found to have very low RSD values with appropriate ranges of 6.16% and 0.095%, respectively.

3.4.6. Regeneration and stability studies. When assessing the effectiveness of biosensors, regeneration and shelf-life are essential considerations. Studies on the interactions between anti-IL8 and IL8 were carried out to evaluate the regeneration capacity of the BSA/anti-IL8/APTES@g-C_3N_4/ITO immunoelectrode. Several regeneration solutions were made, including the fundamental NaOH, acidic HCl or glycine-HCl buffer, and salty $MgCl_2$. The immunological combination of antibody–antigen was also disintegrated in PBS using Tween-20 and a mixture of dimethyl sulfoxide (DMSO) and formamide in a ratio of one to one.[63] The experiment recorded the DPV using a specific IL8 level and the treatment lasted for 30 min [Fig. S6(a)†]. The immunosensor could be used six times, as evidenced by the response obtained after six consecutive regeneration processes [Fig. S6(a)†] showed 75.73% of the original response.

Additionally, during 12 weeks, at weekly intervals, the storage stability of the synthesized immunoelectrode (BSA/anti-IL 8/APTES@g-C_3N_4/ITO) was evaluated in 0.2 M PBS (pH 7.0, 5 mM redox species) [Fig. S6(b)†]. Peak current response variations were tracked using the DPV method. Over a period of ten weeks, the immunoelectrode showed steady current responses, holding onto up to 95% of the initial response. Nevertheless, a sharp decline in peak current was noted after this time. As a result, it was noticed that the immunoelectrode, kept at 4 °C, remained stable for 10 weeks.

3.4.7. Real sample studies. The analysis of IL8 protein in biological samples is becoming an increasingly important task. As a result, the fabricated biosensor was used to measure the amount of IL8 in saliva samples that had been spiked. In this investigation, the BSA/anti-IL8/APTES@g-C_3N_4/ITO immunoelectrode was constructed and the response of real samples, such as saliva, was measured. However, to assess the efficacy of the proposed biosensor in the absence of IL8, genuine saliva samples were spiked with a known amount of IL8 using the conventional addition procedure. The electrochemical response to various spiking doses of IL8 in saliva samples was evaluated using DPV, employing a redox couple and a BSA/anti-IL8/APTES@g-C_3N_4/ITO electrode, as displayed in Fig. 9(a) (the DPV response is magnified in the inset). A consistent pattern of an inverse relationship between the concentration of spiked saliva samples and the recorded response current signal was noted. This pattern remained uniform across all spiked saliva specimens, suggesting a reduction in the amplitude of the response current signal proportional to the elevation in IL8 concentration. The calibration curve illustrating the peak current (mA) plotted against the logarithm of IL8 protein content (ng mL^{-1}) in both PBS and spiked saliva samples for the BSA/anti-IL8/APTES@g-C_3N_4/ITO bioelectrode using the DPV approach is presented in Fig. 9(c). The linear

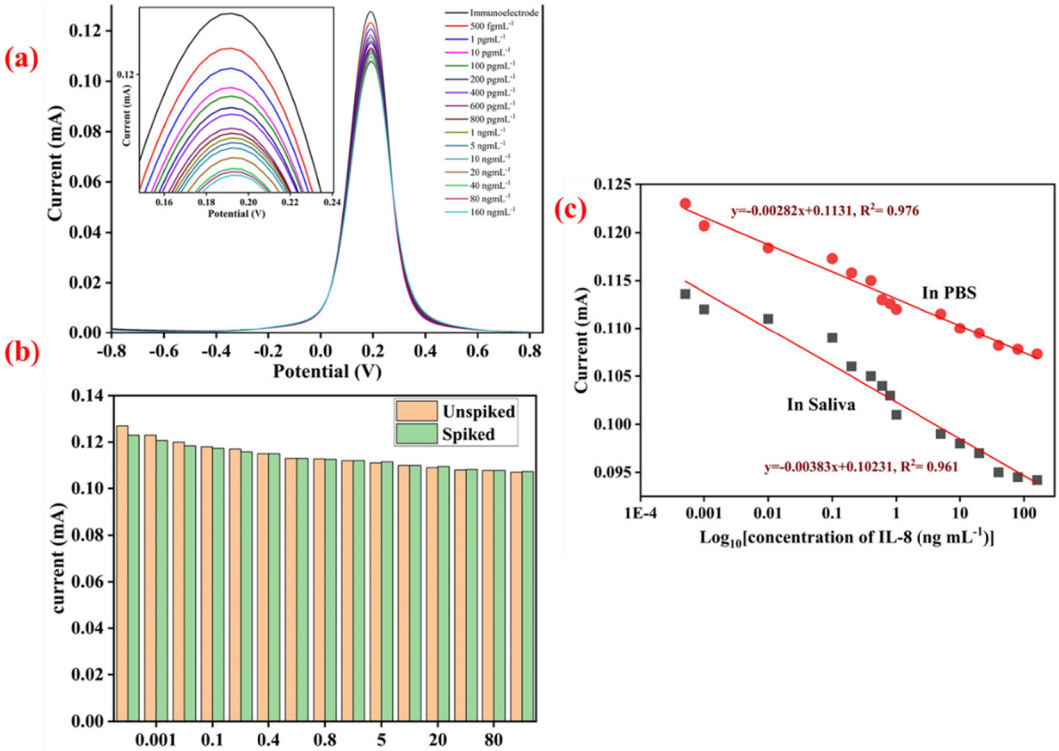

Fig. 9 (a) The constructed immunoelectrode showing the electrochemical DPV responses when IL8 concentrations ranging from 500 fg mL^{-1} to 160 ng mL^{-1} are added in the presence of actual samples; (b) a comparison between the fabricated biosensor current response in the standard and spiked samples; and (c) a calibration curve graph created between the peak current and the IL8 concentrations using both real and standard samples.

Table 4 IL8 recovery rates and the corresponding % RSD values determined using the BSA/anti-IL8/APTES@g-C_3N_4/ITO immunoelectrode with real spiked samples

S. No.	IL8 conc. (ng mL^{-1})	Peak current (mA) in standard samples	Peak current (mA) in spiked saliva samples	% RSD	% Recovery
1	0.0005	0.103	0.113	1.74	91.15
2	0.001	0.112	0.120	0.95	93.33
3	0.01	0.111	0.118	0.42	94.06
4	0.1	0.109	0.117	0.73	93.16
5	0.2	0.106	0.115	0.12	92.17
6	0.4	0.105	0.115	0.09	91.30
7	0.6	0.104	0.112	0.42	92.85
8	0.8	0.101	0.112	0.3	90.17
9	1	0.099	0.111	0.3	89.18
10	5	0.098	0.11	0.5	89.09
11	10	0.097	0.109	0.3	88.9
12	40	0.095	0.108	0.13	87.96
13	80	0.094	0.107	0.5	87.85
14	160	0.094	0.107	0.2	87.85

regression equation below describes the fitted response signals for the IL8 concentrations:

$$I_P = [0.003\ (\text{mA mL ng}^{-1})] \times \log [\text{concentration of IL-8}\ (\text{ng mL}^{-1})] + 0.102 \quad R^2 = 0.961 \tag{9}$$

After quantification, the electrochemical outputs of the fabricated BSA/anti-IL8/APTES@g-C_3N_4/ITO immunoelectrode against varied amounts of standard and spiked saliva samples were detected [Fig. 9(b)]. Regarding IL8, the recovery percentages and RSD range were 87.85–94.06% and 0.09–1.74%, respectively. According to these results, IL8 can be accurately and successfully measured in real samples using the BSA/anti-IL8/APTES@g-C_3N_4/ITO immunoelectrode. Table 4 displays the findings for the RSD and recovery percentage. The results suggest that the BSA/anti-IL8/APTES@g-C_3N_4/ITO immunosen-

sor can be utilized for the early identification of IL8 protein in patient saliva.

4 Conclusions

In summary, an APTES@g-C_3N_4-modified ITO electrode was employed to fabricate an electrochemical immunosensor aimed at detecting IL8. Thermal pyrolysis at a higher temperature was used to synthesize g-C_3N_4, which was then examined using Raman, FT-IR, XRD, FE-SEM, and TEM analysis. The EPD approach was utilized to generate APTES@g-C_3N_4 thin films uniformly on an ITO-coated glass substrate. This allowed for the successful covalent attachment of anti-IL8 through EDC–NHS coupling. EPD was selected due to its affordability, ease of use, and practicality. The modified electrode fabrication efficacy and the antibody–antigen interaction dynamics at the electrode interface were evaluated using CV and DPV methodologies. FT-IR spectroscopy confirmed the conjugation of the antibody onto the electrode interface and morphological characterization was carried out using SEM. Using DPV, the BSA/anti-IL8/APTES@g-C_3N_4/ITO immunoelectrode demonstrated outstanding electrochemical performance throughout a range of IL8 concentrations (500 fg mL^{-1}–160 ng mL^{-1}). The immunosensor outperformed earlier published studies with its exceptional linear range (R^2 = 0.986), high sensitivity (0.015 mA $\log_{10}$ (mL ng^{-1}) cm^{-2}), and a low LOD of 0.04 ng mL^{-1}. The biosensor functioned well in the analysis of saliva samples, yielding satisfactory recovery results. It also showed good specificity and repeatability (RSD = 0.98%) for IL8. The BSA/anti-IL8/APTES@g-C_3N_4/ITO biosensor is a promising tool for measuring IL8 levels, especially in the early stages of cancer detection. It is affordable, specific, stable, and sensitive, and it offers a new method for producing biosensors and biochips that are fast, biocompatible, and extremely sensitive. Further, to translate this research into clinical application, we will further validate the sensitivity and specificity of the BSA/anti-IL8/APTES@g-C_3N_4/ITO biosensor in large and more diverse clinical cohorts to ensure its robust performance across different patient populations. In addition, we will collaborate with clinical researchers to refine the sensor's design and ensure its practical utility in clinical environments. By addressing these steps, we believe that our developed g-C_3N_4 based immunosensor can become a valuable tool in clinical diagnostics, improving patient outcomes through early detection and monitoring of inflammatory conditions.

Nevertheless, residential biosensing systems still lack the necessary precision and dependability in comparison with centralized laboratory-based examination. Significant endeavors have been made to create and construct intelligent biosensing gadgets utilizing artificial intelligence (AI) and internet of things (IoT) techniques. These biosensors serve as adaptable customized healthcare platforms and create new prospects.[64] AI algorithms may enhance the quantitative determination of analytical substances by providing important mathematical tools to analyze the data from biosensing devices. This leads to enhanced accuracy and dependability in the results. In addition, there has been significant interest in biological sensors with IoT integration due of their potential for implementing healthcare 5.0.[65] These biosensing devices have the special capability to be operated and deployed from a distant location. They can detect and provide immediate results on site and also have the capacity to connect to cloud services. This allows for personalized therapy and management for the user or patient.

Live subject statement

Informed consent was obtained from human participants of this study.

Data availability

The data supporting this article have been included as part of the ESI.†

Conflicts of interest

The authors assert that no identifiable conflicting financial interests or personal ties may have impacted any of the research findings presented in this study.

Note after first publication

This article replaces the version published on 11 Jul 2024, which contained errors in Table 1 and the associated discussion.

Acknowledgements

The authors express their gratitude for the characterization facilities offered by the Advanced Instrumentation Research Facility (AIRF) at Jawaharlal Nehru University (JNU). PRS expresses appreciation for the financial support provided by the Indian Council of Medical Research (ICMR), New Delhi, India, and the Biomedical Device and Technology Development (BDTD), Department of Science and Technology (DST), New Delhi, India, for this study. Amit K. Yadav thanks the Prime Minister Research Fellowship, which provides financial assistance under the auspices of the Ministry of Education, Government of India.

References

1 B. W. Neville and T. A. Day, *Ca-Cancer J. Clin.*, 2002, **52**, 195–215.
2 J. Massano, F. S. Regateiro, G. Januário and A. Ferreira, *Oral Surg. Oral Med. Oral Pathol. Oral Radiol. Endod.*, 2006, **102**, 67–76.
3 S. Warnakulasuriya, *Oral Oncol.*, 2009, **45**, 309–316.

4 P. Brocklehurst, O. Kujan, L. O'Malley, G. R. Ogden, S. Shepherd and A.-M. Glenny, *Cochrane Database Syst. Rev*.
5 B. Gupta, A. Ariyawardana and N. W. Johnson, *Int. Dent. J.*, 2013, **63**, 12–25.
6 R. L. Siegel, K. D. Miller, S. A. Fedewa, D. J. Ahnen, R. G. S. Meester, A. Barzi and A. Jemal, *Ca-Cancer J. Clin.*, 2017, **67**, 177–193.
7 L. Wu and X. Qu, *Chem. Soc. Rev.*, 2015, **44**, 2963–2997.
8 G. J. Kelloff and C. C. Sigman, *Nat. Rev. Drug Discovery*, 2012, **11**, 201–214.
9 H. Watanabe, M. Iwase, M. Ohashi and M. Nagumo, *Oral Oncol.*, 2002, **38**, 670–679.
10 K. Xie, *Cytokine Growth Factor Rev.*, 2001, **12**, 375–391.
11 M. A. R. S. John, Y. Li, X. Zhou, P. Denny, C.-M. Ho, C. Montemagno, W. Shi, F. Qi, B. Wu and U. Sinha, *Arch. Otolaryngol., Head Neck Surg.*, 2004, **130**, 929–935.
12 S. Shekhar, A. K. Yadav, A. Khosla and P. R. Solanki, *ECS Sens. Plus*, 2022, **1**(4), 041601.
13 Y. S. Lisa Cheng and J. Wright, *Open Pathol. J.*, 2011, **5**(1), 3–7.
14 R. Mehrotra and D. K. Gupta, *Head Neck Oncol.*, 2011, **3**, 1–9.
15 J. F. Rusling, C. V. Kumar, J. S. Gutkind and V. Patel, *Analyst*, 2010, **135**, 2496–2511.
16 S. B. Nimse, M. D. Sonawane, K.-S. Song and T. Kim, *Analyst*, 2016, **141**, 740–755.
17 N. J. Ronkainen, H. B. Halsall and W. R. Heineman, *Chem. Soc. Rev.*, 2010, **39**, 1747–1763.
18 B. V. Chikkaveeraiah, A. A. Bhirde, N. Y. Morgan, H. S. Eden and X. Chen, *ACS Nano*, 2012, **6**, 6546–6561.
19 S. Kumar, S. Kumar, S. Tiwari, S. Srivastava, M. Srivastava, B. K. Yadav, S. Kumar, T. T. Tran, A. K. Dewan and A. Mulchandani, *Adv. Sci.*, 2015, **2**, 1500048.
20 S. Kumar, M. Umar, A. Saifi, S. Kumar, S. Augustine, S. Srivastava and B. D. Malhotra, *Anal. Chim. Acta*, 2019, **1056**, 135–145.
21 S. Augustine, P. Kumar and B. D. Malhotra, *ACS Appl. Bio Mater.*, 2019, **2**, 5366–5378.
22 X. Li, Y. Li, Q. Qiu, Q. Wen, Q. Zhang, W. Yang, L. Yuwen, L. Weng and L. Wang, *J. Colloid Interface Sci.*, 2019, **543**, 96–105.
23 H. Dai, D. Chen, P. Cao, Y. Li, N. Wang, S. Sun, T. Chen, H. Ma and M. Lin, *Sens. Actuators, B*, 2018, **276**, 65–71.
24 D. Chauhan, V. Nirbhaya, C. M. Srivastava, R. Chandra and S. Kumar, *Microchem. J.*, 2020, **155**, 104697.
25 C. Chaudhary, S. Kumar and R. Chandra, *Microchem. J.*, 2020, **159**, 105344.
26 L. Zhou, X. Zhang, L. Ma, J. Gao and Y. Jiang, *Biochem. Eng. J.*, 2017, **128**, 243–249.
27 Y. Jiang, X. Zhang, L. Pei, S. Yue, L. Ma, L. Zhou, Z. Huang, Y. He and J. Gao, *Chem. Eng. J.*, 2018, **339**, 547–556.
28 S. Kumar, S. Kumar, S. Augustine, S. Yadav, B. K. Yadav, R. P. Chauhan, A. K. Dewan and B. D. Malhotra, *Biosens. Bioelectron.*, 2018, **102**, 247–255.
29 D. Sandil, S. Srivastava, B. D. Malhotra, S. C. Sharma and N. K. Puri, *J. Alloys Compd.*, 2018, **763**, 102–110.
30 S. Zhang, N. Huang, Q. Lu, M. Liu, H. Li, Y. Zhang and S. Yao, *Biosens. Bioelectron.*, 2016, **77**, 1078–1085.
31 F. Mo, J. Xie, T. Wu, M. Liu, Y. Zhang and S. Yao, *Food Chem.*, 2019, **292**, 253–259.
32 S. Zhang, R. Li, X. Liu, L. Yang, Q. Lu, M. Liu, H. Li, Y. Zhang and S. Yao, *Biosens. Bioelectron.*, 2017, **92**, 457–464.
33 K. Mondal, M. A. Ali, C. Singh, G. Sumana, B. D. Malhotra and A. Sharma, *Sens. Actuators, B*, 2017, **246**, 202–214.
34 S. Ansari, M. S. Ansari, H. Devnani, S. P. Satsangee and R. Jain, *Sens. Actuators, B*, 2018, **273**, 1226–1236.
35 S. Ansari, M. S. Ansari, S. P. Satsangee and R. Jain, *Anal. Chim. Acta*, 2019, **1046**, 99–109.
36 S. Ansari, M. S. Ansari, S. P. Satsangee, M. G. Alam and R. Jain, *J. Nanostruct. Chem.*, 2022, 1–15.
37 S. Ansari, M. S. Ansari, S. P. Satsangee and R. Jain, *J. Pharm. Anal.*, 2021, **11**, 57–67.
38 J. Low, B. Cheng, J. Yu and M. Jaroniec, *Energy Storage Mater.*, 2016, **3**, 24–35.
39 A. Wang, C. Wang, L. Fu, W. Wong-Ng and Y. Lan, *Nano-Micro Lett.*, 2017, **9**, 1–21.
40 M. M. Xavier, P. R. Nair and S. Mathew, *Analyst*, 2019, **144**, 1475–1491.
41 H. Liu, X. Wang, H. Wang and R. Nie, *J. Mater. Chem. B*, 2019, **7**, 5432–5448.
42 J. H. Thurston, N. M. Hunter, L. J. Wayment and K. A. Cornell, *J. Colloid Interface Sci.*, 2017, **505**, 910–918.
43 G. Liao, F. He, Q. Li, L. Zhong, R. Zhao, H. Che, H. Gao and B. Fang, *Prog. Mater. Sci.*, 2020, **112**, 100666.
44 A. Kumar, B. Purohit, U. P. Azad, M. T. Yaraki, D. S. Dkhar, Y. N. Tan, A. Srivastava and P. Chandra, *Microchim. Acta*, 2023, **190**, 45.
45 S. Shankar, Y. Kumar, D. Chauhan, N. Sharma, R. Chandra and S. Kumar, *Biosens. Bioelectron.*, 2023, **242**, 115722.
46 S. Shankar, Y. Kumar, D. Chauhan, P. Tiwari, N. Sharma, R. Chandra and S. Kumar, *Microchem. J.*, 2023, **189**, 108555.
47 G. Kalisz, A. Sroka-Bartnicka, R. Nowakowski, M. Naushad, M. B. Gawande, R. Zboril and I. S. Pieta, *ACS Sustainable Chem. Eng.*, 2020, **8**, 1021.
48 D. Das, D. Banerjee, D. Pahari, U. K. Ghorai, S. Sarkar, N. S. Das and K. K. Chattopadhyay, *J. Lumin.*, 2017, **185**, 155–165.
49 J. Liu, T. Zhang, Z. Wang, G. Dawson and W. Chen, *J. Mater. Chem.*, 2011, **21**, 14398–14401.
50 D. C. Poudyal, R. Dugani, B. S. Dash, M. Dhavale, A. K. Satpati and S. K. Haram, *ACS Omega*, 2021, **6**, 13579–13587.
51 M. Shen, L. Zhang, M. Wang, J. Tian, X. Jin, L. Guo, L. Wang and J. Shi, *J. Mater. Chem. A*, 2019, **7**, 1556–1563.
52 A. K. Yadav, D. Verma, A. Kumar, A. N. Bhatt and P. R. Solanki, *Int. J. Biol. Macromol.*, 2023, 124325.
53 D. L. Pavia, G. M. Lampman, G. S. Kriz and J. R. Vyvyan.
54 V. Nirbhaya, C. Chaudhary, D. Chauhan, R. Chandra and S. Kumar, *New J. Chem.*, 2022, **46**, 6201–6211.
55 R. Reverberi and L. Reverberi, *Blood Transfus.*, 2007, **5**, 227.
56 A. K. Yadav, D. Verma and P. R. Solanki, *ACS Appl. Bio Mater.*, 2023, **6**(10), 4250–4268.
57 S. Chandra, C. Gäbler, C. Schliebe, H. Lang and D. Bahadur, *New J. Chem.*, 2016, **40**, 9046–9053.
58 R. Malhotra, V. Patel, J. P. Vaqué, J. S. Gutkind and J. F. Rusling, *Anal. Chem.*, 2010, **82**, 3118–3123.

59 S. Verma, A. Singh, A. Shukla, J. Kaswan, K. Arora, J. Ramirez-Vick, P. Singh and S. P. Singh, *ACS Appl. Mater. Interfaces*, 2017, **9**, 27462–27474.
60 C.-Y. Yang, E. Brooks, Y. Li, P. Denny, C.-M. Ho, F. Qi, W. Shi, L. Wolinsky, B. Wu and D. T. W. Wong, *Lab Chip*, 2005, **5**, 1017–1023.
61 R. M. Torrente-Rodríguez, S. Campuzano, V. R.-V. Montiel, M. Gamella and J. M. Pingarrón, *Biosens. Bioelectron.*, 2016, **77**, 543–548.
62 A. K. Yadav, P. Gulati, R. Sharma, A. Thakkar and P. R. Solanki, *Talanta*, 2022, **243**, 123376.
63 A. Sangili, T. Kalyani, S.-M. Chen, A. Nanda and S. K. Jana, *ACS Appl. Bio Mater.*, 2020, **3**, 7620–7630.
64 A. K. Yadav, D. Verma, A. Kumar, P. Kumar and P. R. Solanki, *Mater. Today Chem.*, 2021, 100443.
65 D. Verma, K. R. B. Singh, A. K. Yadav, V. Nayak, J. Singh, P. R. Solanki and R. P. Singh, *Biosens. Bioelectron.: X*, 2022, **11**, 100153.